NASA Technical Paper 2846

November 1988

Three Component Laser Anemometer Measurements in an Annular Cascade of Core Turbine Vanes With Contoured End Wall

Louis J. Goldman and
Richard G. Seasholtz

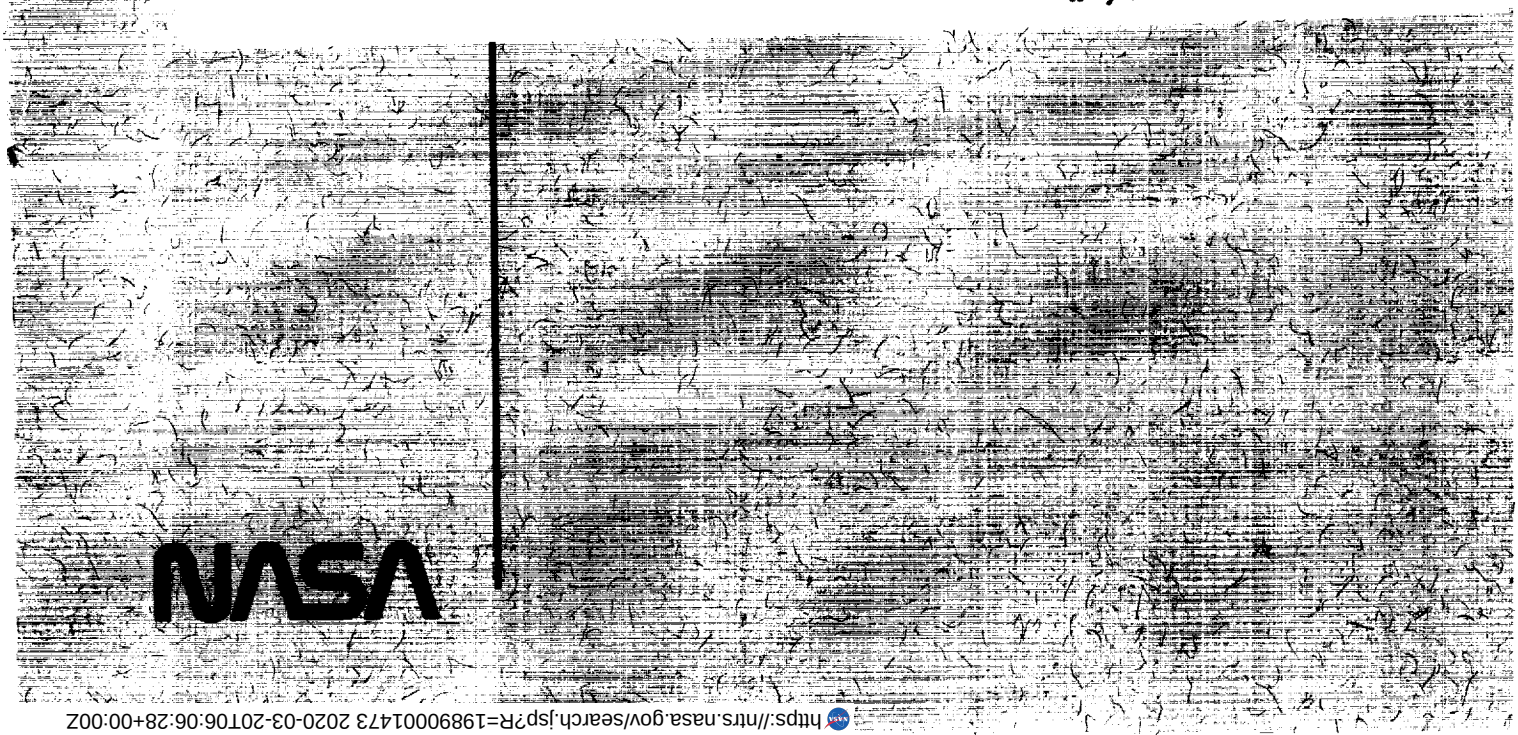

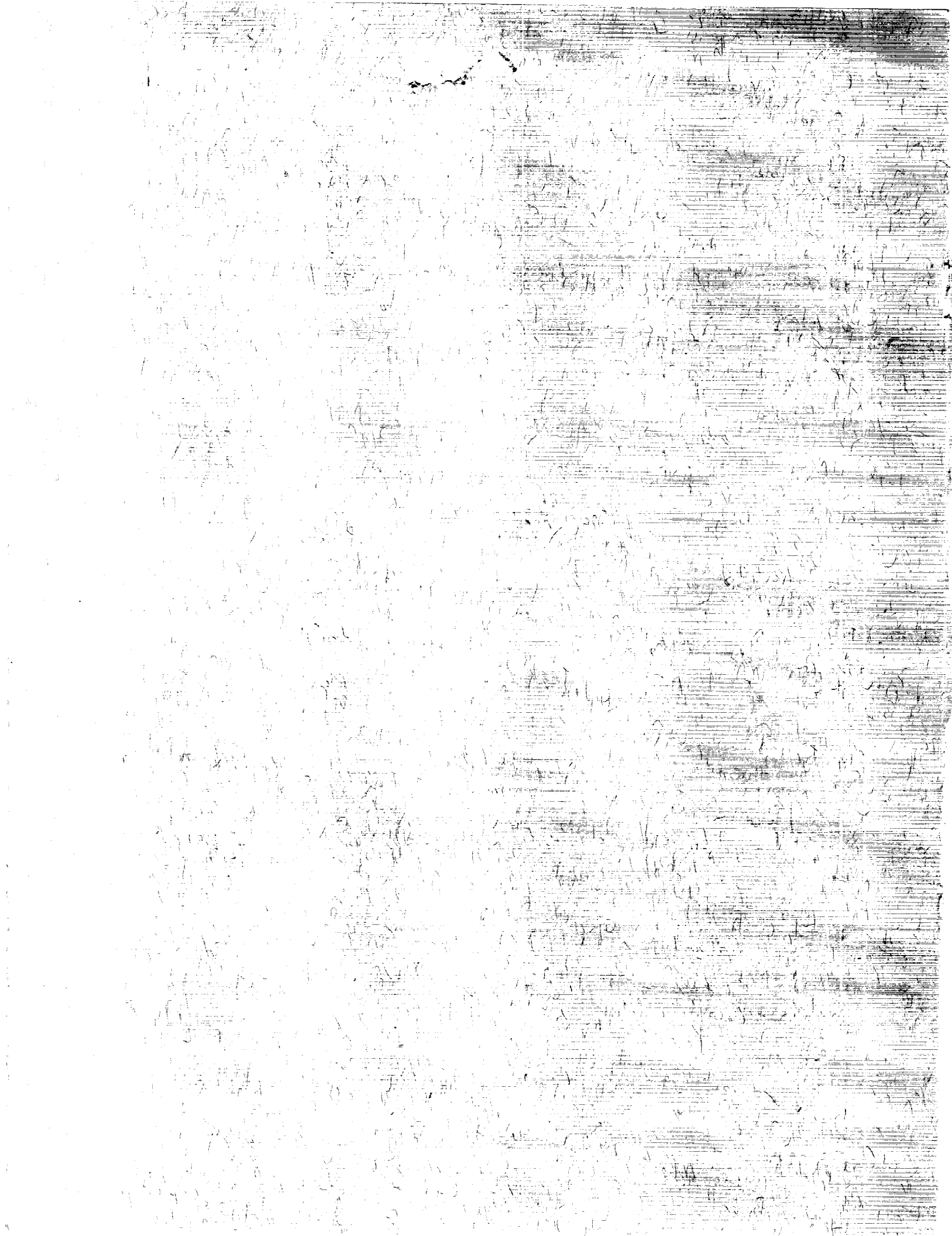

NASA
Technical
Paper
2846

1988

Three Component Laser Anemometer Measurements in an Annular Cascade of Core Turbine Vanes With Contoured End Wall

Louis J. Goldman and
Richard G. Seasholtz
Lewis Research Center
Cleveland, Ohio

National Aeronautics
and Space Administration

Scientific and Technical
Information Division

Summary

The three mean velocity components have been measured in a full-scale annular turbine stator cascade with contoured hub end wall using a newly developed laser anemometer system. The anemometer consists of a standard fringe configuration using fluorescent seed particles to measure the axial and tangential components. The radial component is measured with a scanning confocal Fabry-Perot interferometer. These two configurations are combined in a single optical system that can operate simultaneously in a backscatter mode through a single optical access port. Measurements were obtained both within the stator vane row and downstream of the vanes with the cascade operating at an exit-hub-static- to inlet-total-pressure ratio of 0.724.

The experimental wall static pressure measurements and the laser velocity component measurements were compared with results from the DENTON three-dimensional inviscid computer program. For the static pressure measurements, the agreement was, in general, good except for the hub end wall near the middle of the contour. At this location, the velocity gradients are larger and the theoretical results substantially underpredict the data by about 10 to 20 percent. It is felt that this may have been caused by both inaccuracies in the analytical solution and inaccuracies in the location of the contoured hub end-wall static taps. For the velocity component measurements, the agreement was, in general, reasonable (within 10 percent). The best agreement was found for the radial velocity component, while the poorest was for the tangential velocity component. This may have been caused by seed particle lag problems which would tend to effect the tangential velocity component measurement the most and would result in a lower measured tangential velocity component.

In addition, detailed calibration procedures are described that were used, prior to the experiment, to accurately determine the laser beam probe volume location relative to the cascade hardware.

Introduction

Future advanced aeropropulsion systems will require a substantial improvement in turbomachinery technology. This will depend on the availability of more complex analysis tools to better design these engines. A large effort is underway at the Lewis Research Center, and elsewhere, to develop computer models and programs capable of calculating (1) three-dimensional inviscid and viscous flows, (2) flows with heat transfer, (3) steady and unsteady flows, and (4) single and multistage flows. For the validation of these advanced three-dimensional codes the accurate measurement of all three velocity components in a turbomachinery environment is necessary. Laser anemometry provides a nonintrusive method of obtaining these measurements.

An example of a three velocity component data set for a large-scale turbine-vane passage is presented in reference 1. Unfortunately, for actual size turbomachinery hardware operating at compressible flow conditions, little, if any three component velocity data is available in the open literature. The main reason for this is that, in turbomachinery, one is usually limited to a backscatter configuration with only limited optical access. With these constraints, the standard fringe or time-of-flight anemometer can only accurately measure the velocity components transverse or perpendicular to the optical axis (the tangential and axial components).

Recently, we have described (ref. 2) a backscatter laser system that uses a confocal Fabry-Perot interferometer to directly measure the velocity component along the optical axis (the radial component). When this technique is combined with a conventional fringe-type configuration, as was done in reference 2, the result is a system capable of accurately measuring all three velocity components. To test the capabilities of this system, an existing annular cascade of core turbine stator vanes was modified to produce significant three-dimensional flows. This was accomplished by replacing the cylindrical hub end wall with an s-shaped contoured end wall. Tip end wall contouring was not considered practical because of the difficulty of obtaining optical access for the laser beams. A limited amount of experimental data was presented, in reference 2, to illustrate the ability of this system to measure all three velocity components.

This report is a continuation of the work of reference 2, and presents a complete mapping of the flow within and downstream of the stator. The investigation was performed in a 508-mm tip diameter, ambient-air inlet, annular turbine stator cascade operating at an exit-hub-static- to inlet-total-pressure ratio of 0.724. This pressure ratio, which was greater than the design value of 0.650 for the original cylindrical end-wall configuration, was selected because it prevented supersonic flow from occurring within the vane passage. The subsonic flow field was felt to provide a more reasonable test case for the computer programs in use and under development.

Presented herein, in both graphical and tabulated form, are the results of 25 circumferential surveys taken at constant axial and radial positions within and downstream of the stator. Eleven of these surveys contain radial velocity component measurements which, generally, were obtained only in the region near the contoured hub end wall. For the other regions, the radial velocity was either nearly zero, or the Fabry-Perot signal was much smaller than the signal produced by light scattered off the end wall and could not be separated from it. The experimental measurements are compared, herein, with calculations from the DENTON three-dimensional inviscid computer program described in reference 3. This computer program was previously shown (ref. 4) to give the best comparison (of the three computer codes tested) with the laser anemometer measurements obtained for the same vanes tested with cylindrical end walls.

In addition, detailed calibration procedures are described that were used, prior to the experiment, to accurately determine the laser beam probe volume location relative to the cascade hardware.

Apparatus

Annular Cascade Facility

The 508-mm tip diameter, full-annular, core turbine stator cascade included an inlet section, a test section, and an exit section. A photograph and a cross-sectional view of the facility are shown in figures 1 and 2. In operation, atmospheric air was drawn through the inlet section, the vanes, a dump-diffusing exit section and then exhausted through the laboratory altitude exhaust system. Before entering the altitude exhaust system the flow passed through a flow-straightening section which removed the swirl created by the stator vanes.

Inlet section.—The inlet, consisting of a bellmouth and a short straight section, was designed to accelerate the flow to uniform axial-flow conditions at the vane inlet. The bellmouth profile and coordinates are presented in figure 3. The outer portion of the bellmouth was the same as that used in the cylindrical end wall configuration tests, but the inner portion was a scaled down version of the one used previously. This was done to provide a larger inlet vane height for the s-shaped end wall contour discussed in the next section.

Test section.—The test section, for this investigation, consisted of a sector of four vanes that were part of a full-annular ring of 36 vanes. The annular ring is shown in figure 4 and a schematic cross-sectional view is shown in figure 5. A cutout in the outer vane ring provided access (to the four test vanes) for the laser beams. The test vanes in this region were machined to the vane tip radius in order to permit a window to fit flush with the tip end wall. The window is described in the next section.

The inner or hub end wall contour was s-shaped (fig. 5) with an inlet- to exit-passage-height ratio of 1.25. The geometry and coordinates are shown in figure 5. The outer or tip end wall had a constant diameter of 508 mm and was not contoured, as explained in the Introduction. The s-wall between the four test vanes was polished to a mirrorlike finish to minimize diffuse scattering of the laser beams from this surface.

The stator vane geometry and coordinates are shown in figure 6. The untwisted vanes, of constant profile from hub to tip, were stacked at the center of the trailing-edge circle. These vanes are the same ones tested previously (ref. 5) with the cylindrical end wall configuration of this cascade. Additional geometric information can be found in figure 6 and reference 5. For the tests described herein, two of the test vanes (the ones on the left in fig. 4) were polished to a mirrorlike finish for the same reason as described for the s-wall contour above. The other two test vanes (the ones on the right in fig. 4) were chemically blackened with cupric oxide. This was done to absorb the light scattered off the vanes by the laser beams. It was found that the polished mirrorlike finish was more efficient in minimizing the amount of light scattered off these surfaces.

Windows.—Optical access for the laser beams was provided by cutouts in the test-section outer vane ring (fig. 4) and in the cascade outer housing located downstream of the vane row (fig. 2). Both windows were made from 3.175-mm-thick window glass. They were formed into a cylindrical shape that matched the tip radius by sagging them, in a vacuum furnace, onto a machined graphite form. The form was designed with a recess so that the window area used for the measurements did not touch the form during the sagging process. This was necessary because it was found that areas of the glass that touched the form would pick up the small imperfections in the form and this would degrade the optical properties of the window.

A silicone rubber sealing material was used to seal both windows to the cascade housing and to seal the vane tips to the window. At the vane row, the window covered about 39° in the circumferential direction and was 4 cm high. At the downstream location, the window covered 56° in the circumferential direction and was also 4 cm high.

Laser Anemometer System

A laser anemometer that allows all three velocity components to be measured through a single restricted optical port in a backscatter configuration is described below. The anemometer consists of a standard fringe configuration using a fluorescent aerosol seed to measure the transverse (axial and tangential) velocity components. The radial component is measured with a scanning confocal Fabry-Perot interferometer using the light elastically scattered by the seed particles (i.e., not fluorescence). The two configurations are combined in a single optical system that can operate simultaneously.

Theory.—This section briefly summarizes the results obtained in reference 2, which presented the theory of using two beams of a conventional fringe-type anemometer with an interferometer to measure the optical-axis or radial velocity component.

The scattering geometry for two beams with wave vectors $\mathbf{k}_1$ and $\mathbf{k}_2$ incident on a particle moving with velocity $\mathbf{V}$ is shown in figure 7. (All symbols are defined in appendix A.) For simplicity, the beams are assumed to lie in the r-z plane and have an included angle 2β. (The fringes formed by the beams thus have normals in the z-direction.) The receiving optics aperture is assumed to be an annulus centered on the bisector of the beams with outer radius R_2 and inner radius R_1 and is located a distance f (the lens focal length) from the beam crossing position. The wave vector of the scattered light is $\mathbf{k}_s$ and the optical axis is along the radial direction r.

For the Fabry-Perot interferometer, it has been shown (ref. 2) that the mean values of the Doppler shift frequencies of the elastically scattered light collected over the full annulus are

$$\langle f_{D1,2} \rangle_{FP} = -\frac{1}{\lambda} \left[\pm V_t \sin \beta \cos \alpha + 2(1-\epsilon)\, V_r \right] \quad (1)$$

where

$$\epsilon = 1 - \frac{1}{2} \left[\frac{\sin^2\theta_1 - \sin^2\theta_2}{2(\cos\theta_1 - \cos\theta_2)} + \cos\beta \right]$$

or simplifying,

$$\epsilon = 1 + \frac{1}{4}(\cos\theta_1 + \cos\theta_2) - \frac{1}{2}\cos\beta$$

The value ϵ represents the deviation from pure backscatter and is generally $<<1$. If the scattered light from the two beams is of equal intensity, then the mean value of the frequency of the light scattered from both beams integrated over the annulus is

$$\langle f_D \rangle_{FP} = \frac{1}{2}\left(\langle f_{D1} \rangle + \langle f_{D2} \rangle \right)_{FP} = -\frac{2}{\lambda}(1-\epsilon) V_r \quad (2)$$

Thus, the mean Doppler shift is proportional to the optical-axis or radial velocity component.

For the annular aperture used herein (see ref. 2), $\epsilon = 0.00169$, and the mean value of the Doppler shift frequency given by equation (2) becomes

$$\langle f_D \rangle_{FP} = -\frac{1.9967}{\lambda} V_r \quad (3)$$

For completeness, the mean Doppler frequency for the fringe system is related to the transverse velocity component V_j and fringe spacing s by (ref. 5)

$$\langle f_D \rangle_{Fr} = V_j/s = 2(\sin\beta/\lambda) V_t \cos(\alpha - \phi_j) \quad (4)$$

Optical layout.—A photograph of the laser anemometer and a schematic of the optical layout are shown in figures 8 and 9, respectively. The argon-ion laser was equipped with a temperature controlled etalon and had a maximum output power of 0.8 W at a 514.5-nm wavelength with a vertically polarized TEM_{00} transverse mode and single axial mode.

Lenses L1 and L2 (focal lengths 80 mm and 100 mm, respectively) function as mode-matching lenses to position the beam waists at the focal plane of lens L3. The beam divider (constructed from two appropriately coated 6.35-mm-thick fused silica plates) splits the single beam into two equal intensity parallel beams (approx. 10 mm separation). The divider was mounted in a motor driven rotary mount, so the orientation of the fringes could be set at any desired angle. A half-wave retardation plate (gear driven by the mount at one-half the angle of rotation of the divider) was located at the input of the beam divider to maintain the proper linear polarization at the input of the beam divider.

The two parallel beams from the beam divider were turned by mirrors M3, M4, and M5. Mirror M4 was elliptical with a minor axis of 15.2 mm and major axis of 21.6 mm. This was done to minimize the blockage by the mirror (M4) of the scattered light collected by the receiving optics. The parallel beams were focused by lens L3 (250-mm focal length, 46-mm clear aperture) to cross at the probe volume after being reflected by mirror M5. Mirror M5 was mounted on a motor driven goniometer stage with axis perpendicular to the plane of the optical table. This enabled the optical axis to be positioned along the radial direction in the stator cascade.

The diameter ($1/e^2$ intensity) of the probe volume was about 100 μm and the fringe spacing was 12.93 μm (about eight fringes). The measurement of the fringe spacing is described in appendix B. Light scattered from particles passing through the probe volume (after reflection by M5) was collimated by lens L3. An aperture mask with a central circular stop (diameter, 32 mm) was used to reduce the effective length of the probe volume. This mask blocked 50 percent of the full clear aperture of the collection lens L3, which means the receiving optics had an effective f-number for light collection of $f/6$. The pair of lenses L4 and L5 (focal lengths, 160 mm and 60 mm, respectively) is used to reduce the diameter of the collimated scattered light beam to 17 mm. The beam is then split with a dichroic beam splitter, which reflects 514.5-nm-wavelength light and passes the longer wavelength fluorescent orange light.

After passing through a long wavelength pass filter, LWF, (to remove any residual 514.5-nm light), the fluorescent beam is focused by lens L6 (100-mm focal length) through a 100-μm-diameter pinhole (PH) located in front of photomultiplier PMT1 (RCA 4526). The signal from this PMT is processed by a counter-type processor to provide velocity components transverse to the optical axis.

The light reflected by the dichroic beamsplitter is light elastically scattered by seed particles (i.e., not fluorescence). This 514.5-nm wavelength light is focused by lens L7 (100-mm

focal length) through another 100-μm pinhole and a 16-mm focal length lens (L8, a 10× microscope objective). A narrow band laser line filter (LLF) removes any residual fluorescence and background light before the light enters the confocal Fabry-Perot interferometer (CFPI).

The CFPI has a free spectral range of 3 GHz and a maximum transmission of about 10 percent. The measured finesse (ratio of free spectral range to instrumental bandwidth) was about 50. The light exiting the CFPI was detected by photomultiplier PMT2 (RCA 8850). Photon-counting electronics provided a digital count rate corresponding to the light intensity passed by the CFPI. (Additional factors to be considered in the use of a CFPI for laser anemometry are discussed in ref. 6.)

An acoustic-optic modulator (Bragg cell) was included to generate a reference signal offset from the laser frequency by 400 MHz. The 200-MHz Bragg cell frequency was crystal controlled (second order diffracted beam was used). This signal was used to provide a calibration signal (for data acquisition and data processing) for each sweep of the interferometer. A lens (L9) was used to collimate the beam before the Bragg cell.

Acoustic shielding was necessary to reduce vibration of the laser, which would cause a large jitter in the laser frequency. (The acoustic noise level near the cascade was measured at 105 dB.) The optics and laser were mounted in a wood box covered with a layer of an acoustical foam and lead composite. The weight of the lead shielding used was about 10 kg/m^2.

Positioning system.—The laser and optics were mounted on a 610-mm by 1524-mm by 64-mm-thick aluminum optical breadboard, which was mounted on a three-axis positioning system with a 12-μm positioning accuracy and 1-μm resolution. The positioning system controller was located in the test cell near the cascade with an RS-232 serial communications link to the minicomputer located in the control room. In addition to the three linear stages, the beam divider and goniometer mounted mirror were also controlled with this system. This provided a sufficient number of degrees of freedom to allow the optical axis to be directed along a radial line throughout the test region.

Calibration procedures.—A critical requirement for obtaining laser anemometer data for computer code verification is the accurate determination of the probe volume location relative to the experimental hardware. For the stator cascade described in this paper, location accuracies of 25 μm are desired. A complicating factor in achieving this accuracy is that the stator cascade hardware moves relative to the laser anemometer when going from static to flow conditions and when the ambient temperature changes. Because of these reasons, position calibration must be checked under test conditions. The parameters required are the coordinates of the cascade axes, the radial position of the hub end wall, and the circumferential location of the suction and pressure surfaces of the vanes at a given axial and radial position. The details of the calibration procedures are presented in appendix B.

Seeding.—A fluorescent dye aerosol was used as the seed material for these tests. This material allows measurements (using the technique described in ref. 7) to be made by the LFA part of the system close to the hub, the vanes, and the windows. A liquid dye solution (0.02 molar solution of rhodamine 6G in a 50-50 mixture, by volume, of benzyl alcohol and ethylene glycol) was atomized with a commercial aerosol generator. The aerosol was injected through a 6-mm-diameter tube into the flow at the entrance of the bellmouth.

The fluorescence, because it is broadband, is only usable for the fringe measurements and not for the Fabry-Perot measurements. As a consequence, transverse component measurements could be made closer to surfaces than could radial component measurements. Previous work (ref. 5) in a turbine stator cascade with a similar optical system using fluorescence allowed fringe measurements within 1 mm of the hub (about 2.5 percent of span). The Fabry-Perot measurements could be made to within 3 mm of the hub (about 7.5 percent of span). Because of these constraints, measurements were not made at positions closer than 10 percent of span so that all three velocity components could be obtained.

Test Procedure

Cascade Flow Conditions

The test conditions in the cascade were set by controlling the pressure ratio across the vane row with two throttle valves located in the exhaust system. A hub static tap located downstream of the test section, where the flow was assumed to be nearly circumferentially uniform (station M, fig. 2), was used to set this pressure ratio. For this investigation the exit hub-static to inlet-total pressure ratio $p_{h,M}/P_0$ was maintained at a value of 0.724. This prevented the flow from becoming supersonic within the vane passage. The design pressure ratio for the previously tested (ref. 5) cylindrical hub end wall configuration (no contour) was 0.650 and would have produced supersonic flow within the vane passage had it been used. The subsonic flow field was felt to provide a more reasonable test case for the computer programs in use and under development.

Survey Measurement Locations

The location of the laser survey measurements are summarized in figure 10. Surveys were made at nine axial planes (every 10 percent of axial chord) within the vane passage and at one plane half-axial chord downstream of the vane trailing edge. The nomenclature and orientation of the velocity component measurements are shown in figure 11. At a given axial plane, laser measurements were taken for one or more fixed radial positions between 0.5° to 0.9° circumferential increments across the passage. Twenty-five circumferential surveys were taken, which resulted in about 200 distinct measurement points in the flow field.

At the vane mean radius, measurements were obtained at all 10 axial survey planes. Near the hub and the tip (i.e., radial positions of 10 and 90 percent of span) measurements were made at five axial planes (fig. 10). Near the hub end-wall contour additional measurements were made at radial positions of 20 and 30 percent of span because of the significant radial velocities occurring in this area. Eleven of the twenty five circumferential surveys contain radial velocity measurements.

For the fringe system, at every fixed point in the flow field, seven components of the transverse velocity V_j were measured at 10° intervals centered about the expected flow direction (see fig. 11). This allowed not only the axial and tangential velocity components to be determined but also provided an estimate of their statistical accuracy. For the Fabry-Perot system, it was convenient to obtain radial velocity measurements at each of the seven orientation angles used for the fringe system transverse component measurements. The standard deviation of these seven measurements provides an estimate of the statistical accuracy of the averaged radial velocity component.

Data Acquisition

Two minicomputers were used for experiment control and data acquisition. One minicomputer was used to control the optical positioning system and acquire the fringe anemometer signals. The other computer was dedicated to obtaining the Fabry-Perot signals and, therefore, both sets of signals could be obtained simultaneously. The minicomputers were also used to generate on-line displays of the data so that the system could be monitored for proper operation.

Fringe signal.—The fringe signal from PMT1 was processed with a counter-type processor using four cycles of the Doppler burst. The counter output data, consisting of Doppler frequency and time between measurements, were transferred to the minicomputer via a DMA interface having a maximum transfer rate of about 200 kHz. Data were taken at seven fringe orientations at each measurement position; this being restricted by the 64-kilobyte program size limit of the minicomputer. The fringe orientations were generally selected at 10° intervals and bracketed the predicted flow angle. At each fringe orientation, 1000 data pairs were taken. The frequency data (corresponding to velocity components) were stored in 256 bin histograms for later off-line processing. Typical data rates ranged from 1 to 5 kHz.

Fabry-Perot.—Data were obtained by scanning the Fabry-Perot interferometer over a frequency range that included the laser frequency, the Doppler shifted frequency of light scattered from seed particles, and the Bragg shifted reference frequency. A linear ramp generator, which produced a sawtooth waveform with adjustable period, amplitude, and dc offset, was used to scan the interferometer. The data from the photon-counting electronics were stored in 256 bin histograms; each bin contained the number of counts in 1/256 of the sweep duration. An adjustable number of repetitive sweeps was used to build a composite histogram. Typically, 10 sweeps of 1 sec duration were used. Each sweep was examined by the computer to determine the bin number of the peak corresponding to the Bragg reference signal. The data were then offset to place the Bragg peak at a predetermined bin. This technique was used to eliminate the effect of drift in the laser frequency for data taken over long time intervals. It was found to be desirable to take data over several seconds to reduce biasing caused by short term variations in the rate of seed particles passing through the probe volume. (The observed variation in the data rate was believed to be caused by random cross-flow at the entrance of the bellmouth where the seed was injected.) This procedure was employed for each of the seven fringe orientations used to obtain the fringe measurements. High quality signals were obtained when the data rate was greater than about 10 kHz and values as high as 30 to 50 kHz were not uncommon.

If the radial velocity is near zero (V_r/V_{cr} less than about 0.1), the previous technique is not applicable since the signal from the seed particles overlaps the zero-shift signal from the laser light scattered from the cascade walls. However, the following previously reported (ref. 6) technique can be used. To extract the desired signal, two histograms are constructed: one with the seeding turned on and one with the seeding off. The histograms are subtracted during data processing to give a difference histogram that contains only the desired signal. For the results presented in this report, this technique was generally used for survey measurement points taken farther from the contoured hub end wall.

Calculation Procedures

Experimental

The experimental data obtained from the fringe system and the Fabry-Perot system are quite different and therefore each requires its own calculation procedure. These are described below.

Fringe data.—The fringe data were stored in histogram form—one 256 bin histogram for each fringe orientation at each probe volume position. A typical histogram is shown in figure 12. The mean velocity components V_z and V_θ (see fig. 11) of the projection of the velocity in the axial-tangential plane were obtained by using a two-step procedure. First, each of the histograms (fig. 12) was least-squares fit to a Gaussian function to get estimates of the mean transverse velocity component V_j (using eq. (4) to convert frequency to velocity) as a function of the fringe orientation angle ϕ_j. These Gaussian histogram fits also provided estimates of the variance of the velocity fluctuations s_j^2 as a function of fringe orientation angle ϕ_j.

The second step was to determine the mean axial and tangential velocity components V_z and V_θ. These were found

with a procedure similar to that described in reference 4, where V_z and V_θ are found by using a least-squares fit to

$$V_j = V_z \cos \theta_j + V_\theta \sin \theta_j \tag{5}$$

Typical results of the least-squares procedure is shown in figure 13. The mean transverse velocity magnitude V_t and mean flow angle α can be calculated from

$$V_t = \sqrt{V_z^2 + V_\theta^2} \tag{6}$$

$$\alpha = \arctan\left(\frac{V_\theta}{V_z}\right)$$

For isotropic turbulence, and in the absence of noise from the laser, the turbulence intensity of the flow is calculated from

$$T = \sqrt{v'^2}/V_t \tag{7}$$

where the mean velocity fluctuations v'^2 are obtained by a least-squares fit of

$$s_j^2 = \frac{1}{m}\sum_{j=1}^{m} (V_j - \bar{V}_j)^2 = v'^2\left[1 - \sin 2(\alpha - \phi_j)\right] \tag{8}$$

It has been assumed that α has been determined previously by using equation (6).

Fabry-Perot data.—Typical histograms from the Fabry-Perot interferometer consist of three spectral peaks as shown in figure 14. The right peak is the result of unshifted laser light scattered from surfaces near the probe volume; its amplitude is a function of the position of the probe volume from these surfaces. The left peak is the reference peak from the Bragg cell; it is shifted 400 MHz from the right peak and its amplitude could be controlled by the drive voltage on the Bragg cell. The center peak corresponds to the Doppler-shifted light scattered from the seed particles. Estimates of the frequencies of the three peaks were obtained by a least-squares fit of the data to a three peak Gaussian function. The Doppler-shift frequency of the light scattered from the seed particles is thus proportional to the separation between the center and right peaks. The mean radial velocity component is then calculated from equation (3).

As discussed in the section Test Procedures, if the radial velocity is near zero, the center and the right peaks overlap sufficiently so that two histograms are necessary: one with the seeding turned on and one with the seed off. The histograms are then subtracted to give a difference histogram which contains, under ideal conditions, only the desired signal. A typical set of measurements for this situation is shown in figure 15. The noise from the removed Bragg peaks is still seen in the difference histogram (fig. 15(c)) but the signal corresponding to the radial velocity component is much larger and has the typical Gaussian shape. With the seed turned off (fig. 15(b)) the frequencies of the two peaks are estimated by a least-squares fit of the data to a two peak Gaussian function. As before, the left peak is the reference peak from the Bragg cell and the right peak is the unshifted light scattered from surfaces. The difference histogram data is least-squares fit to a single peak Gaussian function. The difference between the location of this peak and the previously determined right peak is again proportional to the Doppler-shift frequency and the radial velocity component is obtained from equation (3).

Theoretical

The theoretical results for the contoured hub end wall configuration were calculated using the DENTON three-dimensional inviscid computer program described in reference 3. The DENTON program is a time marching finite volume solution of the Euler equations. The static pressure is specified at the downstream hub location and the spanwise pressure variation is calculated by the program assuming zero meridional streamline curvature (simple radial equilibrium). Cusps are placed at the leading and trailing edges of the vanes to minimize discontinuities in the grid slope. The cusps carry no load and, therefore, flow periodicity is automatically satisfied by the program. Of course, the solutions near the vane leading and trailing edges are not realistic.

The DENTON calculations were selected for comparison with the experimental data reported herein because they were previously found (ref. 4) to give the best comparison (of the three computer codes tested) with the fringe system laser measurements obtained for the same vane tested with cylindrical end walls.

Results and Discussion

Surface Static Pressure Measurements

Static pressures were measured on both the vane and end wall surfaces. The vane measurements are presented as critical velocity ratios and are shown in figure 16 for radial positions of 10-, 50-, and 90-percent span. The end wall measurements are presented in figures 17 to 22 for axial positions of 5-, 20-, 40-, 60-, 80-, and 95-percent axial chord. Tabulated pressure ratios are given in tables I and II for about 140 measurement locations.

Comparison of the vane surface measurements and the theoretical results from the DENTON computer program (ref. 3) show good agreement (fig. 16). However, at 50-percent span the measurements tend to be somewhat higher than theory. The results at 10-percent radial span show the influence of the s-shaped hub end wall contour which produces a sharp increase in velocity after 50-percent axial chord.

The comparison of the end wall measurements and theory is also, in general, good except at 80-percent axial chord (fig. 21). At this location the theory substantially underpredicts the measurements by about 10 to 20 percent at the hub end wall. It is felt that this may have been caused by both inaccuracies in the analytical solution and inaccuracies in the location of the contoured hub end wall static taps. For this position, the solution exhibited a total pressure increase of 0.5 to 2.0 percent (for the inviscid calculations the total pressure should be constant). Since the hub contour produces very large changes in velocity with axial position near this location (see fig. 16(c)), the user specified constant axial grid spacing may have been responsible for these analytical inaccuracies. The use of a more concentrated grid, both in the axial and radial directions, tended to result in higher velocity levels at the hub contour and, therefore, better agreement with measurements. In addition, the location of the static taps at 80-percent axial chord may be subject to errors of ± 2 percent because of the curvature of the hub contour. Subsequent measurement of the tap location indicated that they may have been downstream of the 80-percent axial chord position (this measurement is difficult in the vane passage because of the vane turning and the end wall curvature). If the taps were actually at 82-percent axial chord, this would also improve the agreement between the theory and the experiment.

Comparison with Previous Measurements

A limited amount of experimental data was presented previously (ref. 2) to illustrate the ability of a new combined fringe and Fabry-Perot interferometer laser system to measure all three velocity components in an annular turbine stator cascade. After the calibration procedures described in appendix B were completed, experimental measurements were made to check with the results previously reported in reference 2. The comparison between the two data sets is shown in figure 23, where the present measurements are shown as solid symbols. In general, the agreement is good, but slight differences can be noted and may be due to the more complete calibration procedures used for the present data. These results are discussed further in the next section where they are compared with theory.

Survey Measurements

The laser survey measurements are presented in figures 24 to 33 for constant axial planes within the vane passage and for one axial position downstream of the vanes. The experimental data are presented as critical velocity ratios for the three velocity components (axial, tangential, and radial) as a function of circumferential position. These values are also presented in table III. In addition, the circumferential locations of the vane suction and pressure surfaces, which are used in the data presentation figures, are given in table IV. The estimated statistical uncertainty of the measurements (as determined by the methods described in the section Calculation Procedures) are also plotted on these figures as 2σ confidence intervals. If a confidence interval is not shown for a given data point, the 2σ value fell within the symbol used to represent the data point. Also shown on these figures are the theoretical results obtained from the DENTON computer program (ref. 3). The theoretical radial velocity component results are shown on all the figures even when experimental measurements were not obtained. This was done for completeness and to provide, at least, an indication of the level expected for this component.

The results at 10-percent axial chord and 50-percent radial span and 20-percent axial chord and 10-, 50-, and 90-percent radial span are shown in figures 24 and 25, respectively. The comparison of the measurements and the theoretical calculations is very good but the tangential velocity measurements at 20-percent axial chord are slightly lower than the predicted values. The theoretical radial component critical velocity ratio values (figs. 24 and 25) are small, generally less than 0.03. Experimental radial velocity component measurements could not be obtained at these axial positions because the hub end wall is cylindrical at this location and the optical axis is normal to the hub surface. This results in a large signal being produced by light scattering off the end wall (noise) and the small signal due to the radial velocity component could not be separated from this noise. A similar situation also occurs through axial positions of 50-percent axial chord.

The measurements at 30- and 40-percent axial chord and 50-percent radial span are shown in figure 26 and 27, respectively. The comparison between the measurements and theory is good, but again the tangential velocity component measurements are lower than the theory. The measurement uncertainty was found to be larger near the suction surface side of the passage and at 40-percent axial chord the uncertainty is also larger in the middle of the passage.

The data at 50-percent axial chord and 10-, 50-, and 90-percent radial span from the hub are shown in figure 28. The axial velocity component comparisons are considered good while the tangential velocity component comparisons are only fair, particularly, at 10- and 90-percent radial span. Also, the uncertainty in the measurements has increased as can be noted by the increase in the number "error bars" shown in the figure. The contouring of the hub end wall starts just after this axial location and the effect on the theoretical radial velocity component is evident at 10-percent radial span where values of nearly 0.08 occur near the suction surface. Measurements of the radial velocity component, however, could not be obtained for the same reason as discussed previously for the results at 10- and 20-percent axial chord.

The results at 60-percent axial chord and 10-, 20-, 50-, and 90-percent radial span from the hub are shown in figure 29. This was the first axial location where the radial velocity component could be measured. At this position (and positions farther downstream) the hub end wall contouring alleviated the noise problem discussed previously by reflecting the incident laser beams away from the radial direction and thereby from the path of the receiving optics. As discussed in the

section Apparatus, the hub end wall in the test section was hand polished to minimize diffuse scattering from this surface. The radial velocity component measurements agree very well with the theoretical calculations even at 50-percent radial span where the values are less than 0.05. Comparison with the previous axial measurement location, where expected values up to 0.08 could not be measured, indicates the usefulness of the hub contour polishing. At a radial span of 90 percent from the hub, the effect of the hub contouring on the radial velocity component is very small as indicated by the near zero theoretical value. Experimental measurement of the radial velocity component at 90-percent span could not be made at any of the axial measurement positions because of their near zero values.

The comparison of the axial velocity component measurements and theory at 60-percent axial chord is considered good. Only fair agreement is noted for the tangential velocity component comparisons, where again the measurements are lower than the theory. It is felt that this trend of lower tangential velocity component measurements as compared to theory may have been caused by the seed particles lagging the true gas velocity. Previous theoretical calculations for the cylindrical end wall configuration (ref. 5) have shown that particle lag problems would affect the tangential velocity component the most and would result in lower measured values. For the present tests this was a more serious problem because of the use of higher *f*-number optics, which results in less scattered light being collected. The use of higher *f*-number optics resulted from the design constraints imposed by the acoustic enclosure necessary for the Fabry-Perot interferometer. Since the intensity of the scattered light is proportional to the particle size, the size of the seed particles detected by the fringe system for the contoured end wall configuration was probably larger than for the cylindrical end-wall configuration tests, which unfortunately only tends to exacerbate the lag problem. It can also be noted that there are some gaps in the experimental data for radial spans of 10, 20, and 90 percent. These were caused by imperfections in the window which prevented measurements from being obtained due to uncrossing of the laser beams.

The data at 70-percent axial chord and 10-, 20-, 30-, 50-, and 90-percent radial span from the hub are shown in figure 30. The agreement of the radial velocity component measurements and theory is, in general, very good. Large radial velocity components occur near the hub because the s-shaped end wall contour has its maximum slope at 75-percent axial chord (see fig. 10). The comparisons for the axial velocity components are generally good except for the 90-percent radial span position where only fair agreement is noted. At this radial span the axial velocity component measurements tend to be larger than the theoretical calculations. The comparisons for the tangential velocity components are only fair and again the measurements are lower than the theory.

The measurements at 80-percent axial chord and 10-, 20-, 30-, 50-, and 90-percent radial span from the hub are shown in figure 31. The agreement of the radial velocity component measurements and theory are, generally, very good except at 10-percent span. At this radial span the measurements tend to be larger than the theoretical results and the uncertainty of the measurements is bigger near the suction side of the passage. It can also be noted that the three radial velocity measurement points are missing at 30-percent radial span. This was caused by a problem in the data acquisition system resulting in the loss of these data points. The comparisons for the axial velocity components are generally good but the measurements tend to be higher than the theoretical calculations. Similarly, the comparisons are good for the tangential velocity components but again the measurements tend to be lower than the theoretical values.

It might be recalled from the section Surface Static Pressure Measurements that the theoretical calculations substantially underpredicted the measurements at the hub end wall at 80-percent axial chord (fig. 21(b)). This was attributed possibly to the 0.5- to 2.0-percent increase in the total pressure generated by the DENTON code. At radial positions 10-percent span and greater, however, the DENTON code total pressures were usually within 0.25 percent of the ideal values. The agreement with the laser measurements was also much better at these radial locations.

The results at 90-percent axial chord and 50-percent radial span are shown in figure 32. Radial velocity component measurements were not possible at this location for reasons similar to that discussed previously at 10- and 20-percent axial chord. The comparisons for the axial velocity components are good with the measurements again tending to be larger than the theoretical results. The comparisons for the tangential components are fair, with the measurements again being smaller than the theoretical results.

The results at 150-percent axial chord (1/2 axial chord downstream of the vanes) and 50-percent span are shown in figure 33. The comparisons for both the axial and tangential velocity components are, generally, reasonable. Larger measurement uncertainty is noted at this location and was probably caused by diffuse scattering of light off the hub end wall which was not polished downstream of the vanes. Again, the tangential velocity component measurements tend to be lower than the theoretical values. No radial velocity component measurements could be obtained at this location.

In general, the velocity component measurements agreed within 10 percent of the theoretical calculations. This is considered reasonable agreement for this complex three-dimensional flow field.

Turbulence Measurements

A measure of the turbulence intensity at each measurement point is presented in table III. These values were obtained from the fringe system measurements assuming isotropic turbulence and no laser noise, as described in the section Calculation Procedures. In general, the turbulence intensity increases in

passing through the vane passage. On the average, the turbulence level varies from about 3 percent near the vane inlet to around 4.5 percent downstream of the vanes. Similar turbulence levels were measured and reported previously for the cylindrical end wall configuration tests (ref. 5).

Concluding Remarks

The laser anemometer described in this paper has been shown to be capable of measuring the three mean velocity components in a full-scale annular turbine stator cascade with contoured end wall. The addition of a confocal Fabry-Perot interferometer to a conventional fringe-type anemometer allowed the measurement of the radial velocity component with a backscatter configuration. The advantage of this system for turbomachinery research is that it does not require a large optical access port and it is capable of measuring a small radial velocity component when the transverse component is much larger. It also appeared capable of obtaining measurements with smaller sized seed particles than were required for the fringe system.

However, the scanning Fabry-Perot interferometer used herein does have some disadvantages compared to the fringe system used for the transverse velocity measurements. These disadvantages include

1. An increased data acquisition time
2. Requires higher seeding rates
3. An inability to make measurements close to surfaces, particularly, if the optical axis of the anemometer is normal to the surface
4. The need for an acoustic enclosure to protect the laser from high acoustic noise levels
5. An inability to obtain velocity time history information

In addition, the acoustic enclosure tends to compromise the design of the fringe system. This occurs because the enclosure increases the distance between the focusing lens and the facility hardware, resulting in higher *f*-number optics being used. The result is a lower signal-to-noise ratio. Of course, this is not an inherent limitation and the use of larger diameter (lower *f*-number) optics would alleviate this problem.

The experimental wall static pressure measurements and the laser velocity component measurements were compared with the results from DENTON's three-dimensional inviscid computer program. For the static pressure measurements, the agreement was, in general, good except for the hub end wall near the middle of the contour. At this location, the velocity gradients are larger and the theoretical results substantially underpredict the data by about 10 to 20 percent. Possible inaccuracies in both the analytical solution caused by using a constant axial grid spacing in regions of large velocity gradients and errors in the hub end wall static tap location may be the reason for this disagreement. For the velocity component measurements, the agreement was, in general, reasonable (within 10 percent). The best agreement was found for the radial velocity component, while the poorest was for the tangential velocity component. This may have been caused by seed particle lag problems which would tend to affect the tangential velocity component measurement the most and would result in a lower measured tangential velocity component.

In addition, detailed calibration procedures were described that were used, prior to the experiment, to accurately determine the laser beam probe volume location relative to the cascade hardware.

Lewis Research Center
National Aeronautics and Space Administration
Cleveland, Ohio, July 18, 1988

Appendix A
Symbols

A	goniometric stage reading (eq. (10))
$a_{1,2}$	beam divider stage calibration constants (eq. (13))
$b_{1,2}$	goniometric stage calibration constants (eq. (10))
C	beam divider stage reading (eq. (13))
CFPI	confocal Fabry-Perot interferometer
d_{bs}	beam separation (eq. (11))
FP	Fabry-Perot interferometer
Fr	fringe system
f	focal length
f_D	Doppler shift frequency
$f_{D1,2}$	Doppler shift frequencies of light scattered from beams 1 and 2
$\mathbf{k}_s$	wave vector of scattered light
$\mathbf{k}_{1,2}$	wave vectors of incident beams
LFA	laser fringe anemometer (dual-beam laser anemometer)
m	number of transverse velocity component measurements (1000)
PMT	photomultiplier
P_0	inlet total pressure (fig. 2)
$P_{h,M}$	hub static pressure at station M (fig. 2)
$R_{1,2}$	inner and outer radii of annular clear aperture (fig. 7)
r_0	distance from mirror center to probe volume (fig. 36)
s	fringe spacing
s_j^2	variance of the transverse velocity component measurements (eq. (8))
T	turbulence intensity (eq. (7))
$\mathbf{V}$	velocity vector
V_{cr}	critical velocity (fluid velocity at Mach 1)
V_j	measured transverse velocity component (fig. 11)
$\bar{V}_j$	mean value of transverse velocity component
V_r	radial velocity component (fig. 11)
V_t	transverse velocity magnitude (fig. 11)
V_z	axial velocity component (fig. 11)
V_θ	tangential velocity component (fig. 11)
v'	velocity fluctuation
XCON,YCON, ZCON	offset of cascade and positioning system axes (fig. 40)
XREF,YREF, ZREF	offset of reference block and positioning system axes (fig. 43)
x_p,y_p,z_p	positioning system axes (fig. 36)
x_s,y_s	air slit position relative to the positioning system axes (fig. 36)
α	flow angle of transverse velocity with respect to z-axis (fig. 11)
β	one-half beam crossing angle (fig. 7)
ϵ	deviation of mean Doppler shift from true backscatter shift (eq. (1))
θ	angle between optical axis and flow velocity (fig. 7)
θ_s	angle between optical axis and scattered light vector (fig. 7)
$\theta_{1,2}$	angle between optical axis and scattered light vector ending at $R_{1,2}$
λ	laser wavelength
σ	one standard deviation
ϕ_j	fringe orientation angle, angle between z-axis and measured transverse velocity component (fig. 11)
ϕ_s	angular coordinate of scattered light vector (fig. 7)
ψ	goniometric stage rotation angle (fig. 36)
$\langle\,\rangle$	expected value operator

Appendix B
Laser Anemometer System Calibration Procedures

This appendix describes the calibration procedures used to determine the location of the laser beam probe volume relative to the cascade hardware. Complicating this determination is the observation that the cascade hardware can move slightly relative to the laser optics when going from static to flow conditions. Some of the calibration procedures developed could not be used under flow conditions and others were too time consuming to be repeated for each day's run. Therefore, secondary calibration standards were developed and employed to determine these run-to-run changes. Before the location of the probe volume relative to the cascade can be obtained, the position of the probe volume relative to the optics positioning system must be known. Because of this requirement, the calibration of the two rotating stages (beam divider and goniometric) must be accomplished prior to this determination. It is also necessary that these calibrations be performed after all adjustments to the laser optics have been completed. This requires that pinhole adjustments needed to insure coincidence of the effective probe volume locations defined by the fringe and Fabry-Perot receiving optics be done first. Therefore, this appendix is organized in the following manner: (1) Probe Volume Coincidence, (2) Rotating Stage Calibration, (3) Determination of Relative Position of Cascade and Optics (for both static and flow conditions) and, (4) Determination of Probe Volume Location Relative to Vane Passage.

Probe Volume Coincidence

The effective probe volumes defined by the fringe and the Fabry-Perot receiving optics have to be located at the same position in space or the transverse and radial velocity components measured will not correspond to the true velocity vector. This is complicated by the fact that the receiving optics for the fringe system uses the fluorescent (orange) light and the Fabry-Perot system uses the scattered argon (green) light. Pinholes in the two receiving optics (fig. 9) allow adjustments to be made so that the two probe volume measurement locations coincide.

Adjustment of the pinholes during cascade operation was impractical because of the need for the acoustic box, as described previously in the section Laser Anemometer System. To simulate the signals obtained with air flow, a rotating target painted with fluorescent paint (orange) was used. Rotation of the target provided two benefits over a stationary target as follows: (1) imperfections in the painted surface were effectively averaged out and (2) less damage to the painted surface occurred due to the focused laser beams. The probe volume was scanned perpendicular to the wheel surface (parallel to the rotation axis) as shown in figure 34. The laser power was held constant at about 10 mW. The fringe signal was obtained at low PMT power (500 V) to prevent saturation of the PMT. For the Fabry-Perot signal a digital power meter placed in front of the CFPI (fig. 9) was used since this was more convenient than scanning the CFPI for each probe volume position relative to the rotating target. The power meter has adjustable measurement ranges from 2 μW up to 2 W and was also used for most of the calibration procedures described below. The signals obtained from the fringe and Fabry-Perot receiving optics were least-squares fit to separate Gaussian profiles and the determined peak locations were then compared. Typical results before and after adjustment of the fringe system pinhole are shown in figure 35. This technique allowed adjustment of the two probe volume measurement locations to be made to within 25 μm.

Rotating Stage Calibration

As indicated in the section Optical Layout, two rotating stages employed in this laser system were (1) the beam divider stage and (2) the goniometric stage. The beam divider stage allows the orientation of the fringes to be set to any desired angle and therefore determines which component of the transverse velocity is measured. The goniometer stage allows the optical axis to be positioned along the radial direction in the cascade. Similar techniques were used for both stage calibrations.

The first step in the calibration procedure was to obtain an approximate calibration for the beam divider stage. This was accomplished by projecting the two laser beams on a screen located about 15 m from the probe volume. A plumb line was used to provide a vertical reference in front of the screen. The beam divider was then rotated until the two beams intersected the plumb line and the stage position was recorded. The beam divider was then rotated 180° until the two beams again intersected the plumb line and the stage position value was again recorded. A linear calibration of stage position value versus laser beam orientation angle was assumed and this was checked by moving the beams 90° so that the beams would lie in a horizontal plane. The main problem with this technique was that the beam diameter after 15 m is about 100 mm, and it is difficult to determine exactly when the center of the beams intersect the plumb line. Even so, the accuracy of the calibration was estimated to be about $\pm 0.5°$.

The second step in the calibration procedure involved the use of a precision air slit (50 μm $\times$ 3 mm) and a power meter to provide a more quantitative determination of the beam center position. The precision air slit was held in a mounting plate ($50 \times 50 \times 2$ mm) which was attached to the power meter, as shown in figure 36. This setup was then attached to a bracket external to the cascade. The slit was aligned parallel to the positioning systems vertical axis z_p and was located about 140 mm from the probe volume. The calibration technique, as will be seen, is insensitive to the requirement that the axes be parallel.

For the goniometric stage calibration, the laser beams were located (by rotation of the beam divider stage) in the horizontal plane and the laser power was held constant at about 10 mW. At a fixed goniometric stage rotation angle ψ, each of the two beams were individually scanned in the x-direction across the middle (vertical length) of the air slit. The signal from the power meter was least-squares fit to a Gaussian profile for each beam. The peak location obtained from the least-squares procedure defined the center of each beam. By changing the probe volume position relative to the air slit (y-direction) and redoing the x-direction scans, the laser beam directions could be obtained. This allowed the bisector of the beams, or the optical axis, to be determined. Changing the goniometric stage rotation angle ψ and redoing the above procedure resulted in a data set that could be used to obtain the relationship of the goniometric stage values A versus the optical axis position ψ. Actually, much more information can be obtained. For example, the one-half beam crossing angle β can also be determined and, therefore, the fringe spacing can be calculated. Also, the distance from the center of the mirror on the goniometric stage to the probe volume r_0 can be obtained. From the geometry of the beams and air slit shown in figure 36, the following equation, or model function, can be derived

$$x_{p,i} = x_s - r_0 \cos \psi_i - \left[\frac{y_s - y_{p,i} - r_0 \sin \psi_i}{\tan (\psi_i - \text{sgn } \beta)} \right] \tag{9}$$

$$\psi_i = b_1 A_i + b_2 \tag{10}$$

where, the sgn is $+1$ for beam 1 and -1 for beam 2. A six parameter least-squares curve fit was used to obtain the goniometric stage calibration constants b_1 and b_2, one-half beam crossing angle β, the mirror to probe volume distance r_0, and the air slit position x_s, y_s relative to the positioning system axes. The goniometric stage calibration data is shown in figure 37 and indicates that the linear assumption (eq. (10)) was a very good one. The biggest difference between the measured and least-squares value of ψ was 0.03°. Additionally, the least squares procedure gave a one-half beam crossing angle β of 1.140°, corresponding to a fringe spacing of 12.93 μm, and a mirror to probe volume distance r_0 of 188.38 mm.

A similar procedure was used to calibrate the beam divider stage. The vertical air slit was again used and the laser beams in this case were rotated to a given fringe orientation angle ϕ, as shown in figure 38. The goniometric stage was set so that the optical axis was perpendicular to the air slit holder (i.e., $\psi = 90°$). Each of the two beams were again scanned across the middle of the vertical slit. This was accomplished by first moving one of the beams to the middle of the slit (with the positioning system z-stage) and scanning in the x-direction. Afterwards, the second beam was moved to the middle of the slit and the procedure was repeated. The signals from the power meter were again least squares fit to Gaussians to determine the beam centers. The fringe orientation angle ϕ was calculated from

$$\phi = \arcsin \left[\frac{x_{p,1} - x_{p,2}}{d_{bs}} \right] \tag{11}$$

where $x_{p,1}$ and $x_{p,2}$ are the two beam center positions determined from the least-squares fit, and the beam separation d_{bs} *is*

$$d_{bs} = 2(y_s - y_p - r_0) \tan \beta \tag{12}$$

The one-half beam crossing angle β, mirror to probe volume distance r_0, and y-position of the slit y_s were determined during the goniometric stage calibration. The results of the calibration procedure for the beam divider stage are shown in figure 39 plotted with the least-squares linear fit of the data given by

$$\phi_i = a_1 C_i + a_2 \tag{13}$$

Determination of Relative Position of Cascade and Optics

The previous rotating stage calibrations have been in relation to the optics positioning system. This section will explain how the relationship between the cascade and the optics positioning system was determined. Figure 40 shows the coordinate systems for the cascade and the optics positioning system. Initially, the optics positioning system axes were set, using level gauges and micrometer measurements, to be nominally parallel to the cascade axes. The cascade axial direction (z-axis) was nearly vertical. The following procedure was employed to determine the actual relationship between the two coordinating systems.

Rotation of the vane and positioning system axes.—A depth micrometer with two small sections of a razor blade glued to the stem, as shown in figure 41, was placed on the vane leading edges. The stem edge was, therefore, in the axial direction in relation to the plane of the vane leading edges. The razor blade sections extended about 3 mm from the stem and were dulled slightly to provide better light scattering. The micrometer stem position was determined by scanning the laser probe volume in the radial direction. Each of the razor blade sections was then scanned with the laser beams at two or more positions (along the razors edge) to determine the relationship of the vane axial direction z and vane tangential direction x to the positioning system axes. To determine the relationship of the vane radial direction to the positioning systems y-axis the micrometer was placed at two different radial positions; one near the hub and one near the tip. A power meter placed before the CFPI was again used to measure the nonfluorescent

scattered laser light from the razor edge and the micrometer stem. The signals were least-squares fit to Gaussians and the peak locations determined the razor edge or micrometer stem location. Typical scans across the razor blade are shown in figure 42, which indicates that the vane tangential direction is within ± 25 μm of the positioning system x-axis. Similarly, it was found that the relationship between the vane axial and radial directions and the positioning systems z- and y-axes were also within this tolerance. This corresponds to about a $\pm 1/4°$ rotation of the vane and positioning system axes, and no corrections were applied.

Translation of the vane and positioning system axes.— The depth micrometer with the razor blade section was also used to obtain the position of the vane leading edge with respect to the positioning system. The depth micrometer was set to a given value and with the razor blade thickness measured to be 0.25 mm, the razor edge location relative to the vane leading edge was therefore known. The peak location of the laser beam scan (in the z-direction) across the razor blade gave the relationship ZCON (see fig. 40) between the vane tangential direction and the positioning system x-axis. The relationships, XCON and YCON, (fig. 40) between the two coordinate systems were found by determining the cascade center position. This was accomplished by scanning the laser beams in the radial direction and determining the hub end wall position (on the noncontoured part of the end wall) for different circumferential positions. A least-squares fit to a Gaussian gave the hub positions which were then least-squares fit to a circle to determine the cascade center and the constants XCON and YCON. The above procedures were all done in a static (no-flow) environment and were not practical for use under flow conditions. To determine changes in the coordinate system relationships (i.e., XCON, YCON, and ZCON) during cascade operation (with flow), a simpler procedure was employed. This procedure was followed for each days run and is described below.

A small block ($7 \times 25 \times 20$ mm) was fastened to the cascade flange (external to the flow path) and was set parallel to the optics positioning systems axes. Two small razor blade sections were glued to the block as shown in figure 43. This system was, therefore, very similar to the depth micrometer setup described previously. After the positioning system relationships (XCON, YCON, and ZCON) were established (by the previously described procedures), the external block was scanned with the laser beams sequentially across the two razor sections and perpendicular to the block face. Least-squares fits to Gaussians were again used to determine the position of the block face and the positions of the two razor blade sections with respect to the positioning system axes. These values (XREF, YREF, and ZREF; see fig. 43) were recorded and compared to similar scans taken during cascade operation (with flow). Any differences in these values were assumed to be due to translation of the coordinate system axes and appropriate changes in XCON, YCON, and ZCON were made in the positioning systems computer control program. Typical changes in the values of XCON, YCON, and ZCON were found to be less than 100 μm in going from static to flow conditions in the cascade.

Determination of Probe Volume Location Relative to Vane Passage

The final step in the calibration procedure was to determine the probe volume location relative to the test passage geometry during cascade operation. This was done at the beginning of each days run. At a given axial position (where laser anemometer measurements were to be made) a radial scan of the laser beams was performed to determine the hub end wall location. Again, the signal was least-squares fit to a Gaussian and the peak value located the hub end wall. This not only provided a check of the previous calibration techniques, but subsequent radial positions used for the velocity component measurements were made relative to this determined hub value. To determine the vane surface location, circumferential scans of the laser beams were performed at constant radial positions. A least-squares fit of the data to a Gaussian profile gave the circumferential position θ of the vane surface. Subsequent circumferential positions used for the velocity component measurements were made relative to the value determined for the suction surface of the vane. This completed the calibration procedure and the system was now ready to obtain velocity component measurements.

References

1. Bailey, D.A.: Study of Mean- and Turbulent-Velocity Fields in a Large Scale Turbine-Vane Passage. NASA CR-3067, 1979.
2. Seasholtz, R.G.; and Goldman, L.J.: Combined Fringe and Fabry-Perot Laser Anemometer for Three Component Velocity Measurements in Turbine Stator Cascade Facility. Advanced Instrumentation for Aero Engine Components, AGARD CP-399, AGARD, Nevilly-Sur-Seine, France, 1986, pp. 13-1 to 13-15. (Also, NASA TM-87322.)
3. Denton, J.D.: An Improved Time Marching Method for Turbomachinery Flow Calculation. J. Eng. Power, vol. 105, no. 3, July 1983, pp. 514-524.
4. Goldman, L.J.; and Seasholtz, R.G.: Comparison of Laser Anemometer Measurements and Theory in an Annular Turbine Cascade with Experimental Accuracy Determined by Parameter Estimation. Engineering Applications of Laser Velocimetry, H.W. Coleman and P.A. Pfund, eds., ASME, 1982, pp. 83-92. (Also, NASA TM-82860.)
5. Goldman, L.J.; and Seasholtz, R.G.: Laser Anemometer Measurements in an Annular Cascade of Core Turbine Vanes and Comparison With Theory. NASA TP-2018, 1982.
6. Seasholtz, R.G.; and Goldman, L.J.: Laser Anemometer Using a Fabry-Perot Interferometer for Measuring Mean Velocity and Turbulence Intensity along the Optical Axis in Turbomachinery. Engineering Applications of Laser Velocimetry, H.W. Coleman and P.A. Pfund, eds., ASME, 1982, pp. 93-101. (Also, NASA TM-82841).
7. Stevenson, W.H.; dos Santos, R.; and Mettler, S.C.: Fringe Mode Fluorescence Velocimetry. Applications of Non-Intrusive Instrumentation in Fluid Flow Research, AGARD CP-193, AGARD, Nevilly-Sur-Seine, France, 1976, pp. 20-1 to 20-9.

TABLE I.—VANE SURFACE STATIC PRESSURE MEASUREMENTS AT TEST PRESSURE RATIO OF 0.724

Radial position, R, percent span	Axial position, Z, percent chord	Suction surface pressure ratio, p_s/P_0	Pressure surface pressure ratio, p_p/P_0
10	5	0.949	-----
	10	.919	0.980
	20	.909	.983
	30	.890	.980
	40	.872	.975
	50	.863	.967
	60	.804	.959
	70	.690	.930
	80	.632	.868
	90	.663	.789
	95	.699	.735
	97.7	.725	-----
50	5	0.918	-----
	10	.873	0.979
	20	.863	.981
	30	.812	.976
	40	.770	.968
	50	(a)	.955
	60	.729	.935
	70	.720	.902
	80	.703	.854
	90	.703	.804
	95	.722	.771
	97.7	.741	-----
90	5	0.920	-----
	10	.858	0.976
	20	.838	.978
	30	.772	.974
	40	.725	.966
	50	.727	.954
	60	.736	.933
	70	.753	.904
	80	.745	.866
	90	.742	.819
	95	.761	.788
	97.7	.774	-----

[a]Static tap partially plugged.

TABLE II.—END WALL SURFACE STATIC PRESSURE MEASUREMENTS AT TEST PRESSURE RATIO OF 0.724

Axial position, Z, percent chord	Hub circumferential position, θ_H, deg	Hub end wall pressure ratio, p_h/P_0	Tip circumferential position, θ_T, deg	Tip end wall pressure ratio, p_t/P_0
5	12.17	0.956	9.94	0.903
	13.30	.961	11.10	.935
	14.43	.965	12.25	.951
	15.56	.974	13.40	.961
	16.68	.976	14.56	.967
	17.81	.983	15.71	.972
	18.94	.984	16.87	.976
20	12.51	0.940	10.22	0.854
	13.64	.951	11.42	.910
	14.77	.961	12.62	.936
	15.89	.971	13.83	.952
	17.02	.976	15.03	.963
	18.15	.981	16.23	.972
40	11.91	0.918	9.66	0.775
	13.13	.932	10.73	.851
	14.35	.952	11.81	.895
	15.57	.964	12.89	.923
	16.78	.971	13.97	.940
	-----	-----	15.04	.956
60	9.75	0.874	7.96	0.742
	10.96	.897	9.05	.774
	12.17	.927	10.13	.817
	13.38	.951	11.22	.858
	14.59	.966	12.31	.890
	-----	-----	13.40	.918
80	6.00	0.571	5.08	0.744
	7.14	.608	6.12	.754
	8.29	.667	7.16	.766
	9.44	.729	8.20	.779
	10.59	.779	9.24	.796
	11.73	.816	10.28	.817
	-----	-----	11.32	.850
95	2.18	0.661	1.81	0.750
	3.35	.654	2.88	.745
	4.52	.643	3.95	.745
	5.68	.656	5.02	(a)
	6.85	.678	6.10	.766
	8.02	.693	7.17	.781
	9.19	.725	8.24	.801
	-----	-----	9.32	.805

[a]Static tap partially plugged.

TABLE III. – LASER VELOCITY MEASUREMENTS FOR CORE TURBINE STATOR VANES WITH CONTOURED END WALL AT TEST PRESSURE RATIO OF 0.724

Survey number	Axial position, Z, percent axial chord	Radial position, R, percent span	Circumferential position, θ, deg	Axial component critical velocity ratio, V_z/V_{cr}	Standard deviation in axial component, σ_{V_z}/V_{cr}	Tangential component critical velocity ratio, V_θ/V_{cr}	Standard deviation in tangential component, σ_{V_θ}/V_{cr}	Radial component critical velocity ratio, V_r/V_{cr}	Standard deviation in radial component, σ_{V_r}/V_{cr}	Turbulence intensity, T, percent
1	10	50	16.60	0.178	0	0.069	0.001	-----	-----	2.9
			15.89	.191		.068	0	-----	-----	2.7
			15.17	.207	↓	.067	.001	-----	-----	2.8
			14.46	.224		.058	.001	-----	-----	2.7
			13.75	.241	.001	.051	.002	-----	-----	2.6
			13.03	.257	.001	.036	.002	-----	-----	2.7
			12.32	.275	.001	.019	.003	-----	-----	2.9
			11.60	.290	.002	−.013	.003	-----	-----	4.2
2	20	10	15.64	0.200	0	0.079	0	-----	-----	2.8
			15.04	.215	.001	.073	.001	-----	-----	2.9
			14.44	.231	.001	.064	.001	-----	-----	2.8
			13.84	.249	.001	.055	.002	-----	-----	2.6
			13.24	.264	.002	.051	.003	-----	-----	2.7
			12.64	.292	.002	.034	.003	-----	-----	3.6
3	20	50	15.58	0.202	0	0.090	0	-----	-----	2.7
			14.78	.223	.001	.087	.002	-----	-----	2.2
			13.98	.244	.002	.083	.004	-----	-----	2.5
			13.18	.269	.002	.076	.004	-----	-----	2.7
			12.38	.303	.002	.055	.004	-----	-----	3.5
			11.58	.353	.007	.011	.012	-----	-----	3.8
4	20	90	15.10	0.220	0.001	0.089	0.003	-----	-----	2.9
			14.30	.239	.001	.087	.003	-----	-----	2.8
			13.50	.261	.001	.082	.003	-----	-----	3.1
			12.70	.290	.002	.079	.005	-----	-----	3.9
			11.90	.339	.003	.054	.008	-----	-----	3.8
			11.10	.381	.002	.047	.006	-----	-----	2.9
5	30	50	15.54	0.202	0	0.116	0	-----	-----	3.2
			14.88	.221	.001	.116	.002	-----	-----	2.9
			14.21	.241	.002	.115	.004	-----	-----	3.0
			13.54	.263	.001	.116	.002	-----	-----	3.6
			12.88	.299	.003	.114	.005	-----	-----	4.4
			12.21	.351	.004	.095	.008	-----	-----	3.4
			11.54	.386	.005	.104	.008	-----	-----	3.2
6	40	50	15.05	0.211	0.002	0.147	0.003	-----	-----	2.9
			14.30	.231	.002	.153	.003	-----	-----	3.3
			13.55	.263	.003	.158	.003	-----	-----	4.3
			12.80	.315	.005	.156	.007	-----	-----	3.6
			12.05	.352	.007	.169	.010	-----	-----	3.0
			11.30	.387	.005	.204	.006	-----	-----	3.8
			10.55	.487	.004	.213	.006	-----	-----	3.7

TABLE III.—Continued.

Survey number	Axial position, Z, percent axial chord	Radial position, R, percent span	Circumferential position, θ, deg	Axial component critical velocity ratio, V_z/V_{cr}	Standard deviation in axial component, σ_{V_z}/V_{cr}	Tangential component critical velocity ratio, V_θ/V_{cr}	Standard deviation in tangential component, σ_{V_θ}/V_{cr}	Radial component critical velocity ratio, V_r/V_{cr}	Standard deviation in radial component, σ_{V_r}/V_{cr}	Turbulence intensity, T, percent
7	50	10	14.50	0.196	0.002	0.166	0.002	-----	-----	3.0
			13.70	.211	.002	.180	.002	-----	-----	3.4
			12.90	.249	.005	.184	.005	-----	-----	4.1
			12.10	.298	.005	.196	.005	-----	-----	3.5
			11.30	.326	.009	.221	.009	-----	-----	3.1
			10.50	.326	.004	.290	.004	-----	-----	3.6
8	50	50	14.56	0.215	0.002	0.183	0.002	-----	-----	3.6
			13.73	.253	.007	.198	.008	-----	-----	4.3
			12.90	.307	.005	.211	.006	-----	-----	4.4
			12.06	.323	.006	.246	.007	-----	-----	2.8
			11.23	.377	.005	.265	.006	-----	-----	4.2
			10.40	.446	.007	.316	.008	-----	-----	3.4
			9.56	.466	.007	.403	.008	-----	-----	3.9
9	50	90	14.03	0.233	0.005	0.190	0.006	-----	-----	3.6
			13.20	.288	.009	.196	.011	-----	-----	3.7
			12.37	.315	.004	.221	.005	-----	-----	2.7
			11.53	.348	.005	.247	.005	-----	-----	3.2
			10.70	.425	.005	.255	.006	-----	-----	4.3
			9.87	.476	.009	.305	.010	-----	-----	3.0
			9.03	.516	.010	.395	.012	-----	-----	4.0
10	60	10	13.52	0.189	0.004	0.208	0.003	[a]0.072	0.004	4.0
			12.72	.213	.003	.232	.002	[a].078	.012	4.7
			11.92	(b)	-----	-----	-----	-----	-----	-----
			11.12	.286	.016	.270	.012	[a].056	.018	3.5
			10.32	.283	.009	.318	.007	[a].119	.007	4.6
			9.52	.301	.013	.374	.010	[a].149	.007	4.6
11	60	20	13.50	0.220	0.005	0.220	0.004	[a]0.046	0.003	4.8
			12.83	.268	.011	.229	.009	[a].061	.005	3.9
			12.17	.275	.009	.256	.007	[a].066	.008	3.3
			11.50	(b)	-----	-----	-----	-----	-----	-----
			10.83	.278	.007	.332	.005	[a].085	.001	4.0
			10.17	.352	.008	.348	.006	.095	.008	4.8
			9.50	.371	.009	.395	.007	.083	.014	3.6
12	60	50	13.49	0.254	0.008	0.243	0.006	[a]0.025	0	3.8
			12.74	.289	.010	.257	.008	[a].028	.002	3.1
			11.99	.302	.005	.286	.004	[a].037	.010	3.8
			11.24	.351	.010	.322	.008	[a].045	.002	5.2
			10.49	.401	.006	.345	.005	[a].047	.005	4.0
			9.74	.412	.011	.399	.008	[a].036	.001	3.3
			8.99	.407	.007	.470	.005	[a].045	.006	4.4

[a]Difference histogram.
[b]Bad spot on window; measurements could not be made.

TABLE III.—Continued.

Survey number	Axial position, Z, percent axial chord	Radial position, R, percent span	Circumferential position, θ, deg	Axial component critical velocity ratio, V_z/V_{cr}	Standard deviation in axial component, σ_{V_z}/V_{cr}	Tangential component critical velocity ratio, V_θ/V_{cr}	Standard deviation in tangential component, σ_{V_θ}/V_{cr}	Radial component critical velocity ratio, V_r/V_{cr}	Standard deviation in radial component, σ_{V_r}/V_{cr}	Turbulence intensity, T, percent
13	60	90	13.48	0.260	0.006	0.237	0.005	-----	-----	3.8
			12.65	.293	.012	.258	.009	-----	-----	3.1
			11.82	.323	.011	.263	.009	-----	-----	4.0
			10.98	.364	.009	.305	.007	-----	-----	4.9
			10.15	(b)	-----	-----	-----	-----	-----	-----
			9.32	.438	.013	.395	.010	-----	-----	3.7
			8.48	.455	.014	.466	.011	-----	-----	4.4
14	70	10	12.46	0.235	0.009	0.272	0.007	0.097	0.008	4.0
			11.74	.234	.008	.318	.006	.123	.004	3.0
			11.03	.252	.005	.335	.004	.134	.002	3.3
			10.32	.274	.009	.369	.007	.152	.003	4.3
			9.60	.322	.014	.397	.010	.168	.004	4.2
			8.89	.345	.011	.431	.009	.199	.009	3.7
			8.17	.337	.016	.478	.012	.253	.023	3.2
15	70	20	12.45	0.253	0.004	0.296	0.003	[a]0.082	0.004	2.8
			11.70	.265	.007	.325	.005	.093	.003	3.2
			10.95	.296	.007	.352	.005	.103	.003	4.3
			10.20	.343	.013	.387	.010	.119	.006	4.2
			9.45	.363	.008	.423	.006	.129	.003	3.5
			8.70	.361	.014	.471	.011	.145	.007	3.4
			7.95	.372	.010	.528	.008	.161	.003	4.0
16	70	30	12.45	0.253	0.008	0.315	0.006	[a]0.057	0.005	2.7
			11.70	.277	.006	.333	.005	[a].066	.001	3.8
			10.95	.324	.009	.359	.007	[a].074	.004	4.6
			10.20	.363	.011	.398	.008	[a].085	.004	3.7
			9.45	.358	.007	.442	.005	.091	.003	3.3
			8.70	.339	.021	.490	.008	.097	.008	5.2
			7.95	.389	.009	.530	.007	.100	.004	3.7
17	70	50	12.46	0.259	0.007	0.321	0.005	[a]0.031	0.008	2.9
			11.56	3.01	.005	.344	.004	[a].035	.002	4.4
			10.66	.358	.011	.377	.009	[a].037	.008	4.2
			9.76	.376	.009	.426	.007	[a].045	.006	3.2
			8.86	.370	.008	.481	.006	[a].040	.003	3.4
			7.96	.392	.012	.521	.009	[a].049	.006	4.0

[a]Difference histogram.

[b]Bad spot on window; measurements could not be made.

TABLE III.—Continued.

Survey number	Axial position, Z, percent axial chord	Radial position, R, percent span	Circumferential position, θ, deg	Axial component critical velocity ratio, V_z/V_{cr}	Standard deviation in axial component, σ_{V_z}/V_{cr}	Tangential component critical velocity ratio, V_θ/V_{cr}	Standard deviation in tangential component, σ_{V_θ}/V_{cr}	Radial component critical velocity ratio, V_r/V_{cr}	Standard deviation in radial component, σ_{V_r}/V_{cr}	Turbulence intensity, T, percent
18	70	90	11.85	0.275	0.008	0.327	0.006	-----	-----	3.3
			11.10	.338	.010	.330	.008	-----	-----	4.8
			10.35	.395	.011	.343	.008	-----	-----	4.2
			9.60	.406	.013	.385	.010	-----	-----	3.1
			8.85	.405	.006	.429	.005	-----	-----	3.7
			8.10	.394	.011	.474	.009	-----	-----	4.7
			7.35	.415	.018	.524	.014	-----	-----	4.1
19	80	10	11.41	0.266	0.006	0.363	0.005	0.122	0.007	3.8
			10.70	.316	.014	.400	.011	.141	.002	4.3
			9.98	.349	.009	.434	.007	.157	.004	3.6
			9.27	.353	.010	.475	.008	.170	.005	3.4
			8.55	.378	.008	.497	.006	.185	.003	4.3
			7.84	.402	.006	.534	.005	.194	.005	4.2
			7.13	.418	.017	.563	.013	.223	.022	3.9
			6.14	.415	.009	.621	.007	.258	.009	3.9
20	80	20	11.39	0.290	0.012	0.373	0.009	[a]0.079	0.011	4.3
			10.68	.331	.010	.406	.008	.090	.008	4.1
			9.96	.334	.007	.445	.005	.109	.005	3.4
			9.25	.362	.009	.467	.007	.113	.004	3.5
			8.53	.392	.014	.504	.011	.117	.007	4.3
			7.82	.396	.011	.544	.008	.126	.005	3.8
			7.10	.401	.012	.571	.010	.128	.005	3.8
			6.39	.389	.007	.617	.006	.132	.004	3.9
21	80	30	11.50	0.294	0.012	0.377	0.009	[a]0.056	0.003	4.2
			10.76	.337	.010	.406	.008	[a].069	.006	4.1
			10.02	.348	.006	.443	.005	[a].075	.001	3.3
			9.27	.362	.010	.467	.007	[a].078	.003	3.4
			8.53	.380	.008	.504	.006	[a].078	.006	4.3
			7.79	.381	.010	.547	.007	(c)	-----	3.7
			7.04	.380	.008	.588	.006	-----	-----	3.5
			6.30	.371	.006	.619	.005	-----	-----	3.6
22	80	50	11.39	0.307	0.014	0.384	0.010	[a]0.021	0.007	4.3
			10.68	.339	.009	.413	.007	[a].037	.001	3.7
			9.96	.346	.012	.446	.009	[a].030	.007	3.2
			9.25	.357	.010	.479	.008	[a].036	0	3.4
			8.53	.371	.006	.500	.004	[a].041	.001	3.8
			7.82	.380	.010	.531	.008	[a].034	.009	3.8
			7.10	.372	.011	.558	.009	[a].043	.002	3.6
			6.39	.366	.011	.583	.008	[a].044	.004	3.5

[a]Difference histogram.
[c]Data acquisition problem; measurements lost.

TABLE III.—Concluded.

Survey number	Axial position, Z, percent axial chord	Radial position, R, percent span	Circumferential position, θ, deg	Axial component critical velocity ratio, V_z/V_{cr}	Standard deviation in axial component, σ_{V_z}/V_{cr}	Tangential component critical velocity ratio, V_θ/V_{cr}	Standard deviation in tangential component, σ_{V_θ}/V_{cr}	Radial component critical velocity ratio, V_r/V_{cr}	Standard deviation in radial component, σ_{V_r}/V_{cr}	Turbulence intensity, T, percent
23	80	90	11.48	0.311	0.011	0.371	0.009	-----	-----	4.4
			10.77	.345	.010	.392	.007	-----	-----	4.2
			10.05	.366	.009	.419	.007	-----	-----	3.3
			9.34	.373	.008	.442	.006	-----	-----	3.2
			8.62	.367	.009	.481	.007	-----	-----	3.6
			7.91	.390	.009	.493	.007	-----	-----	4.1
			7.20	.393	.011	.526	.008	-----	-----	3.7
			6.48	.383	.012	.547	.009	-----	-----	3.6
24	90	50	9.79	0.334	0.010	0.457	0.007	-----	-----	3.3
			9.04	.355	.010	.468	.007	-----	-----	3.3
			8.29	.348	.009	.489	.007	-----	-----	3.2
			7.54	.337	.015	.516	.011	-----	-----	3.5
			6.79	.341	.009	.539	.006	-----	-----	3.6
			6.04	.344	.013	.561	.009	-----	-----	3.6
			5.29	.336	.013	.582	.009	-----	-----	3.1
25	150	50	20.51	0.267	0.013	0.551	0.007	-----	-----	5.3
			20.01	.266	.012	.553	.007	-----	-----	4.8
			19.51	.294	.016	.580	.009	-----	-----	4.8
			19.01	.287	.012	.572	.007	-----	-----	4.3
			18.51	.286	.007	.575	.004	-----	-----	4.0
			18.01	.289	.010	.577	.006	-----	-----	3.8
			17.51	.283	.010	.576	.006	-----	-----	3.9
			17.01	.284	.011	.585	.007	-----	-----	3.6
			16.51	.285	.009	.585	.005	-----	-----	3.7
			16.01	.281	.011	.587	.006	-----	-----	3.7
			15.51	.308	.015	.573	.008	-----	-----	3.9
			15.01	.260	.027	.597	.015	-----	-----	3.4
			14.51	.325	.025	.569	.015	-----	-----	4.3
			14.01	.296	.013	.587	.008	-----	-----	3.8
			13.51	.295	.011	.592	.006	-----	-----	3.8
			13.01	.283	.013	.597	.008	-----	-----	3.9
			12.51	.277	.012	.597	.007	-----	-----	4.1
			12.01	.292	.017	.585	.010	-----	-----	4.1
			11.51	.287	.019	.578	.011	-----	-----	4.8
			11.01	.268	.008	.569	.004	-----	-----	5.4
			10.51	.279	.011	.558	.007	-----	-----	5.4
			10.01	.251	.014	.574	.008	-----	-----	5.5
			9.51	.286	.016	.587	.009	-----	-----	6.5
			9.01	.292	.014	.580	.008	-----	-----	4.4
			8.51	.292	.010	.589	.006	-----	-----	5.6
			8.01	.277	.009	.593	.005	-----	-----	4.4
			7.51	.288	.009	.583	.005	-----	-----	4.5
			7.01	.289	.012	.589	.007	-----	-----	3.7
			6.51	.304	.012	.586	.007	-----	-----	3.8
			6.01	.303	.011	.586	.006	-----	-----	3.9
			5.51	.292	.014	.593	.008	-----	-----	3.8

[a]Difference histogram.
[c]Data acquisition problem; measurements lost.

TABLE IV.—VANE CIRCUMFERENTIAL LOCATIONS USED FOR DATA PRESENTATIONS

Axial position, Z, percent chord	Radial position, R, percent span from hub	Suction surface position, θ_S, deg	Pressure surface position, θ_P, deg
5	0	11.45	19.25
	100	9.30	17.51
10	50	10.50	18.04
20	0	11.80	18.49
	10	11.54	18.30
	50	10.58	17.61
	90	9.77	17.03
	100	9.59	16.90
30	50	10.43	17.02
40	0	11.14	16.99
	50	9.99	16.27
	100	9.06	15.68
50	10	10.04	15.87
	50	9.21	15.39
	90	8.51	14.97
60	0	8.91	14.86
	10	8.72	14.76
	20	8.53	14.65
	50	8.01	14.37
	90	7.42	14.05
	100	7.28	13.97
70	10	7.01	13.48
	20	6.87	13.41
	30	6.73	13.35
	50	6.48	13.22
	90	6.02	12.99
80	0	5.20	12.11
	10	5.10	12.07
	20	5.00	12.04
	30	4.91	12.00
	50	4.74	11.93
	90	4.43	11.80
	100	4.36	11.77
90	50	2.63	10.57
95	0	1.46	9.85
	100	1.24	9.87

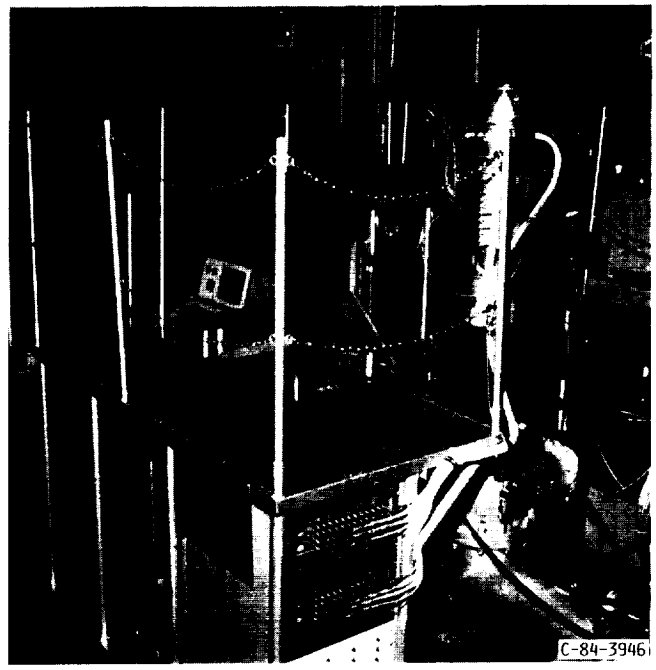

Figure 1.—Turbine stator cascade facility.

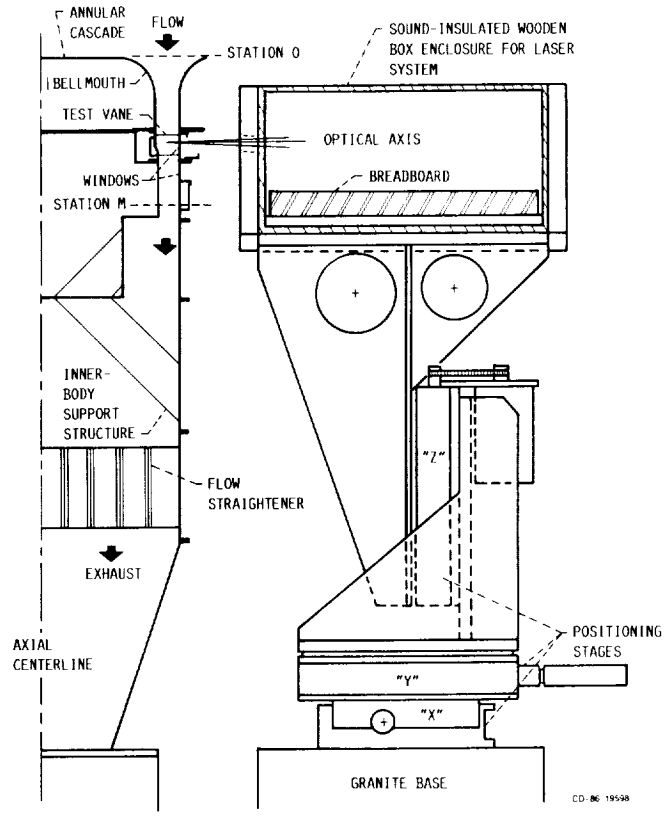

Figure 2.—Schematic cross-sectional view of core turbine stator cascade and laser positioning system.

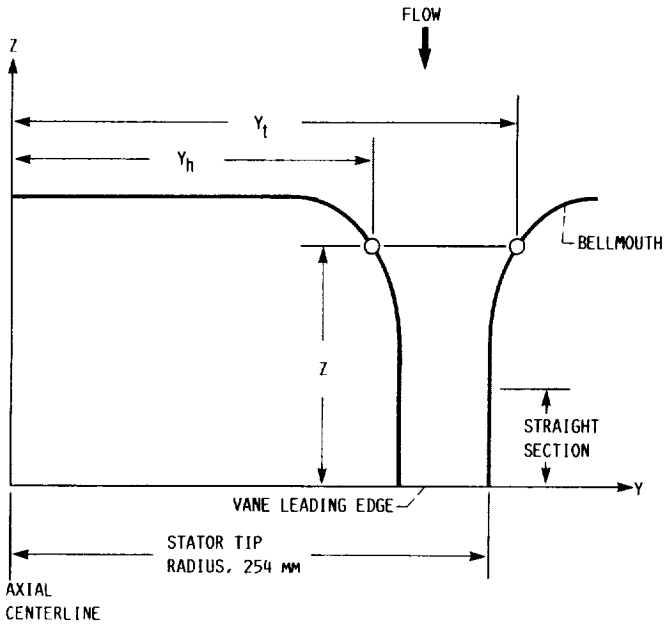

Z	Y_h	Y_t
0	0.813	1.000
.200	.813	1.000
.266	.812	1.001
.293	.811	1.002
.331	.808	1.005
.360	.804	1.008
.385	.800	1.013
.406	.795	1.018
.425	.789	1.024
.443	.783	1.030
.458	.776	1.036
.473	.769	1.043
.498	.755	1.058
.520	.739	1.074
.539	.722	1.091
.556	.704	1.109
.574	.676	1.136
.588	.648	1.165
.594	.629	1.184
.598	.590	1.203
.600	.582	1.231

(ALL VALUES NONDIMENSIONALIZED BY STATOR TIP RADIUS, 254 MM.)

Figure 3.—Annular cascade inlet bellmouth geometry.

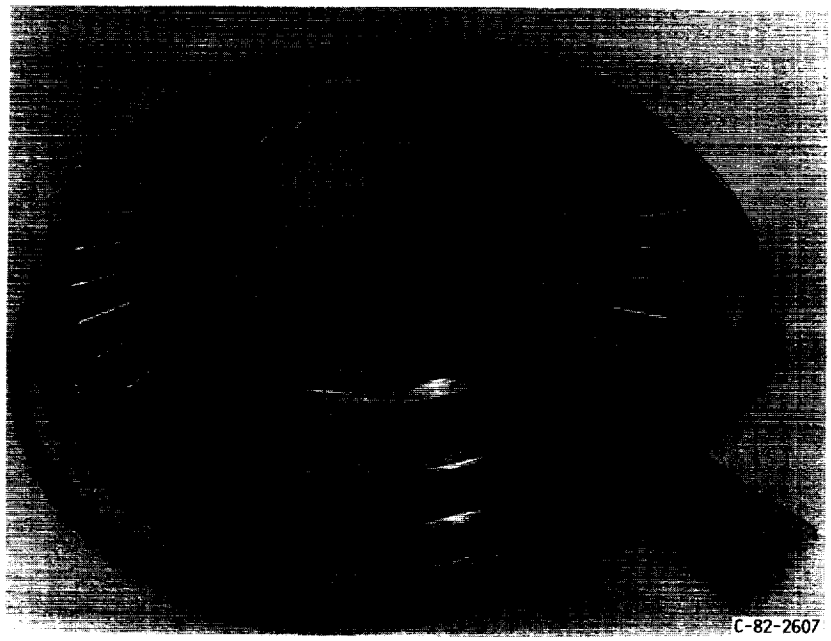

Figure 4.—Annular vane ring.

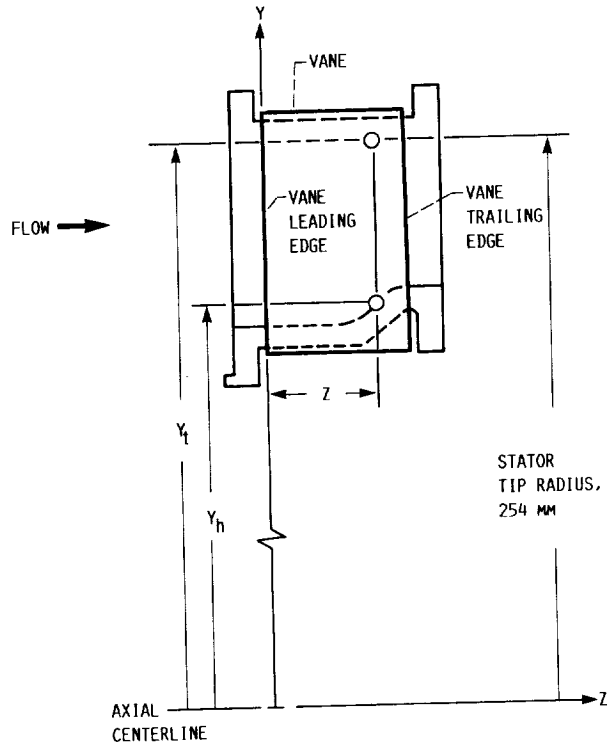

Z	Y_h	Y_t
0	0.813	1.000
.076	.813	
.085	.813	
.094	.816	
.101	.820	
.107	.825	
.113	.831	
.119	.837	
.125	.842	
.133	.847	
.142	.850	
.151	.850	1.000

(ALL VALUES NONDIMENSIONALIZED BY STATOR TIP RADIUS, 254 MM.)

Figure 5.—Contoured hub end wall geometry.

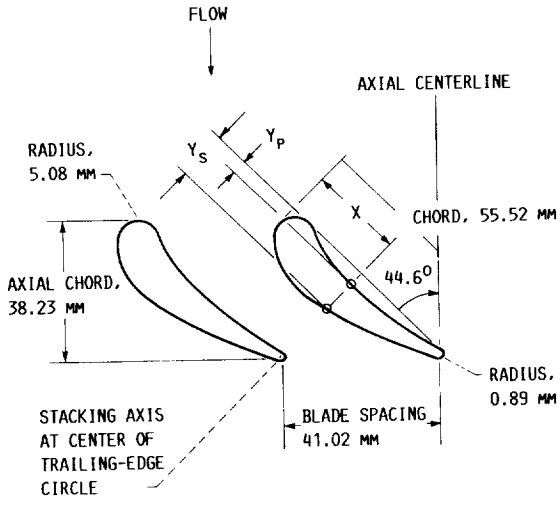

X	Y_P	Y_S
0	0.091	0.091
.023	—	.153
.046	—	.181
.069	—	.202
.091	—	.218
.114	—	.231
.137	.011	.242
.160	.021	.250
.183	.029	.257
.206	.036	.261
.229	.043	.263
.252	.048	.265
.274	.053	.266
.320	.059	.263
.366	.065	.257
.412	.068	.248
.457	.069	.238
.503	.069	.226
.549	.066	.215
.595	.064	.200
.640	.059	.185
.686	.054	.170
.732	.047	.153
.778	.040	.134
.823	.032	.114
.869	.023	.094
.915	.015	.072
.961	.005	.048
1.000	.016	.016

(ALL VALUES NONDIMENSIONALIZED BY CHORD, 55.52 MM.)

Figure 6.—Core turbine stator vane geometry at mean section.

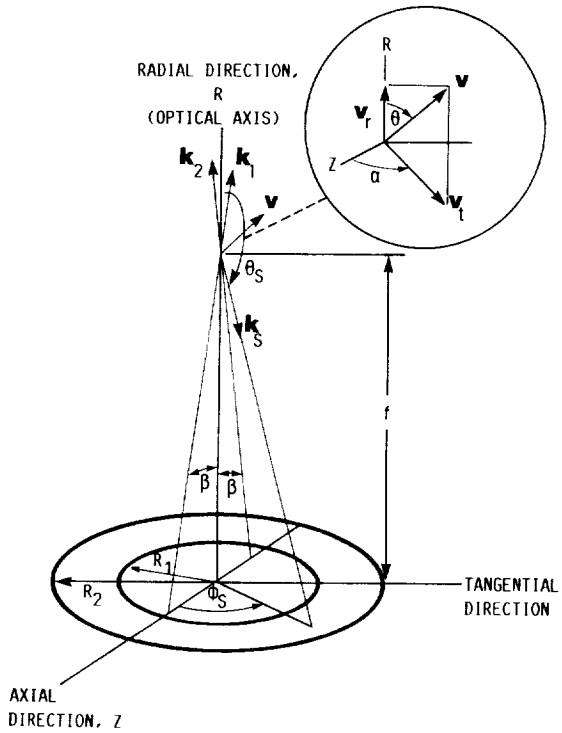

Figure 7.—Scattering geometry.

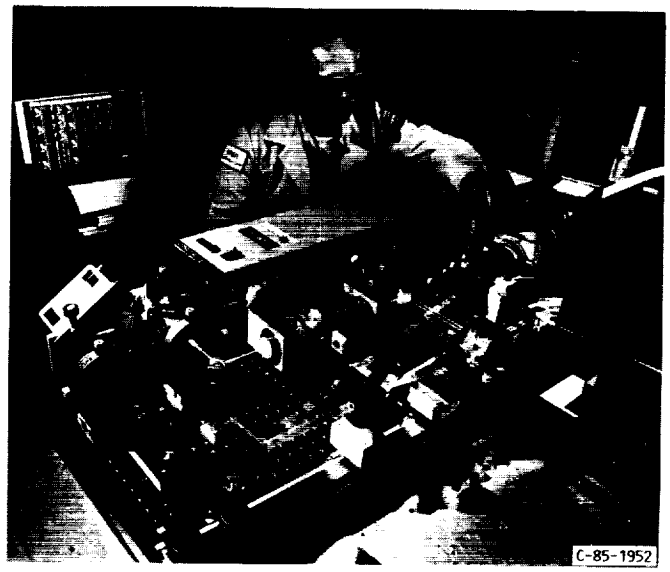

Figure 8.—Three component laser anemometer.

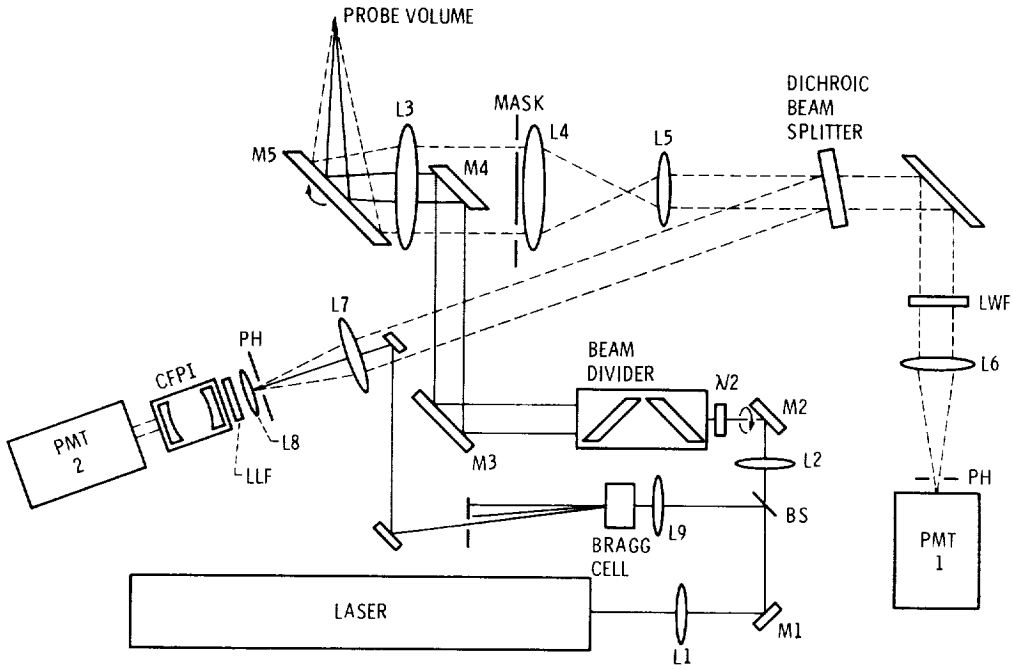

Figure 9.—Optical layout.

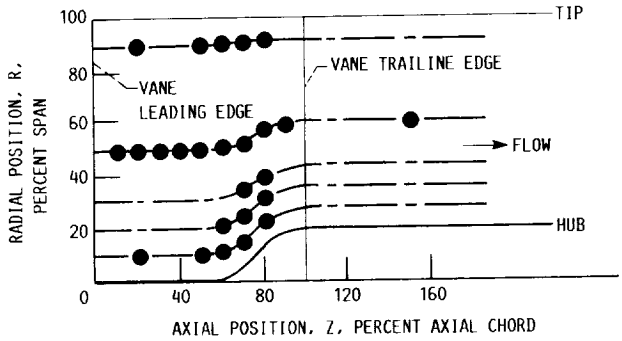

Figure 10.—Laser survey measurement locations.

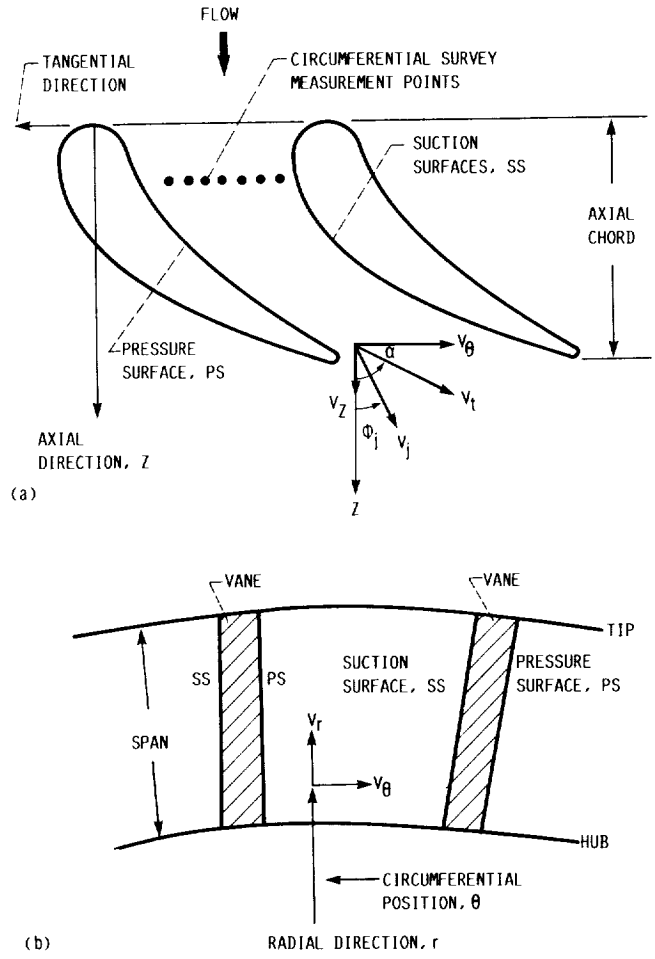

(a) Blade-to-blade view.
(b) Passage cross-sectional view.
(c) Coordinate system and velocity components.

Figure 11.—Nomenclature and orientation of velocity component measurements for laser anemometer surveys.

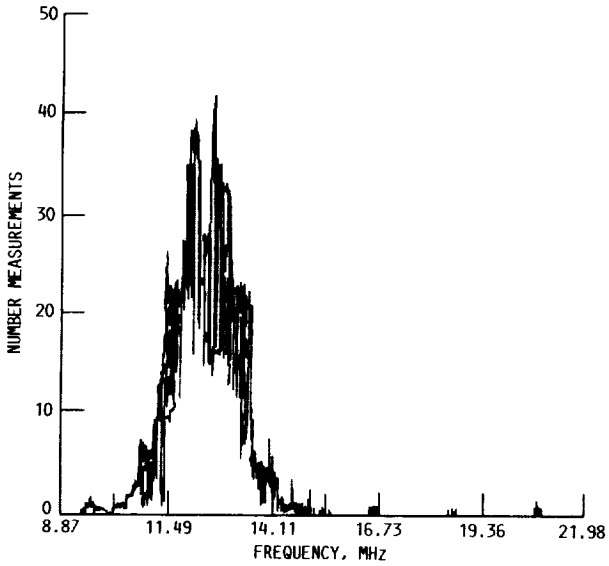

Figure 12.—Fringe data histogram.

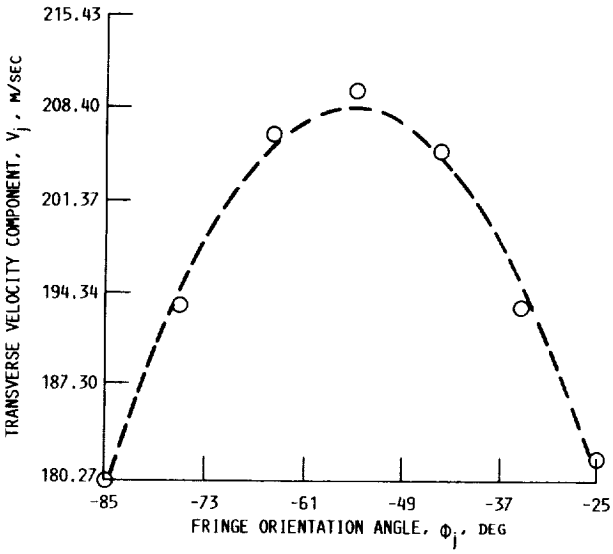

Figure 13.—Least-squares fit of velocity component measurements.

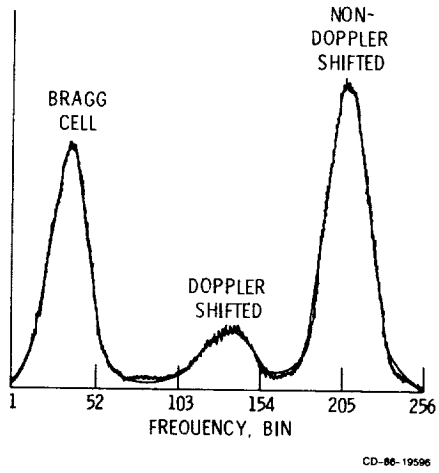

Figure 14.—Fabry-Perot spectrum for large radial velocity component.

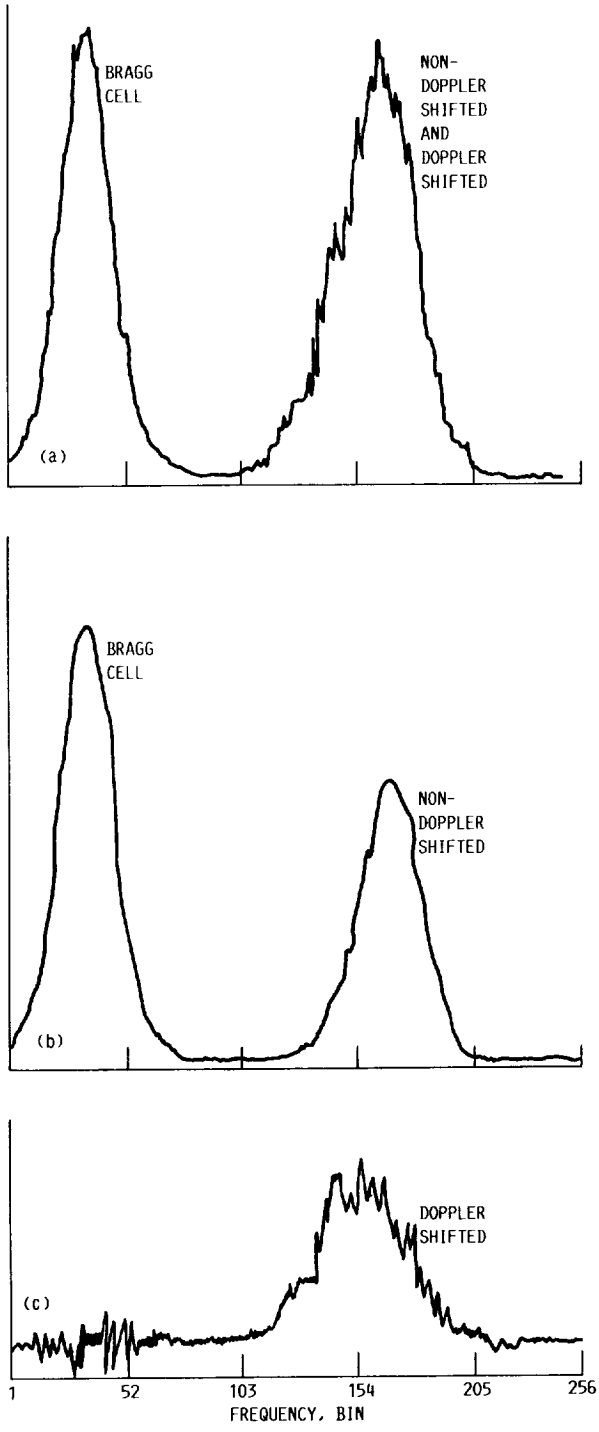

(a) Seeded flow histogram.
(b) Unseeded flow histogram.
(c) Difference histogram.

Figure 15.—Fabry-Perot spectrum for small radial velocity component.

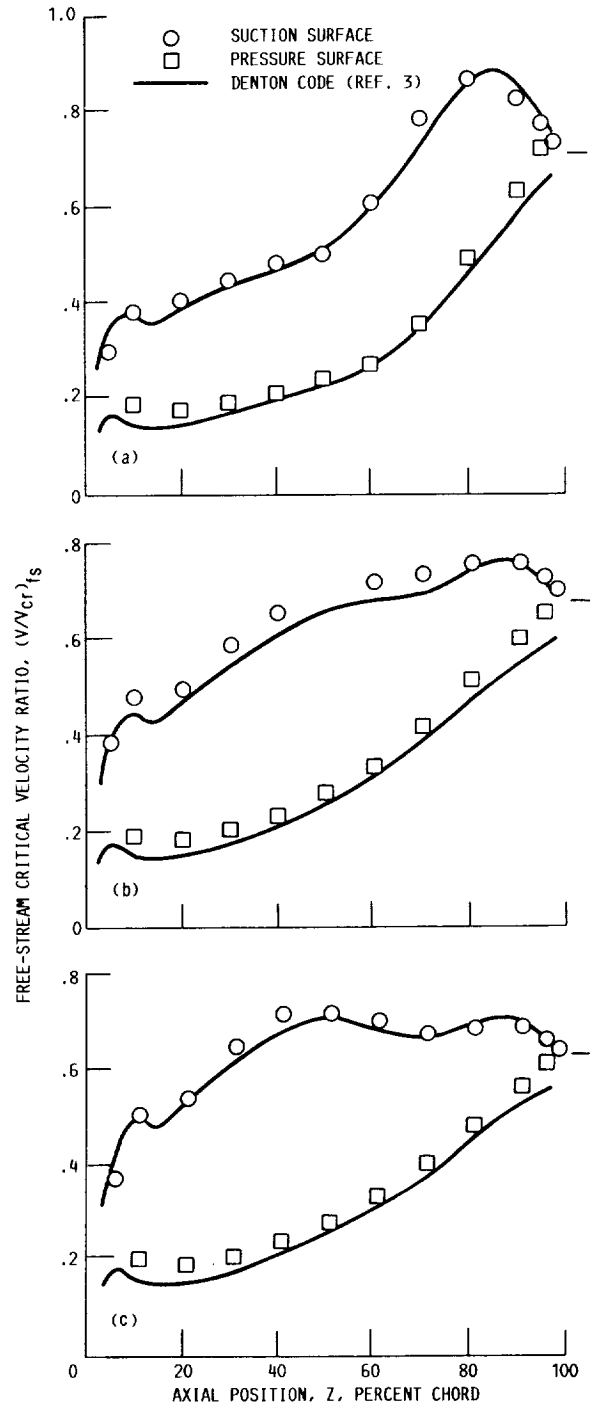

(a) Radial position R, 90-percent span from hub.
(b) Radial position R, 50-percent span from hub.
(c) Radial position R, 10-percent span from hub.

Figure 16.—Distribution of free-stream critical velocity ratio around vane at pressure ratio, $p_{h,M}/P_0$, of 0.724. (Velocities calculated from surface static pressure measurements.)

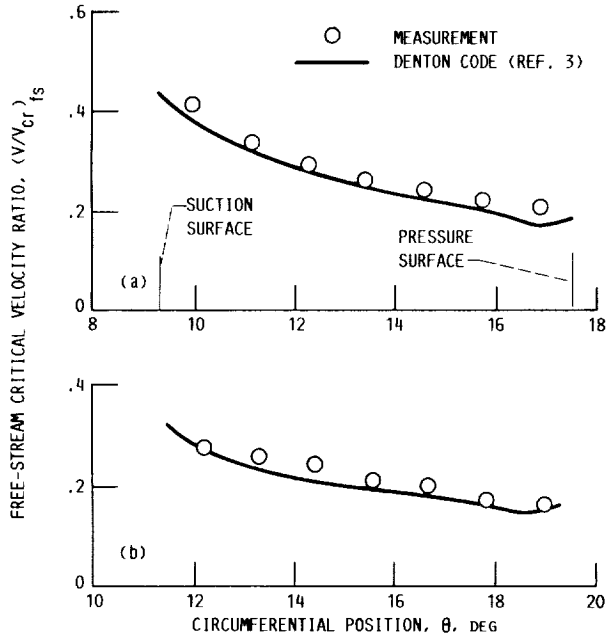

(a) Tip end wall.
(b) Hub end wall.

Figure 17.—Distribution of free-stream critical velocity ratio on end walls at an axial position of 5-percent axial chord and a pressure ratio, $p_{h,M}/P_0$, of 0.724. (Velocities calculated from surface static pressure measurements.)

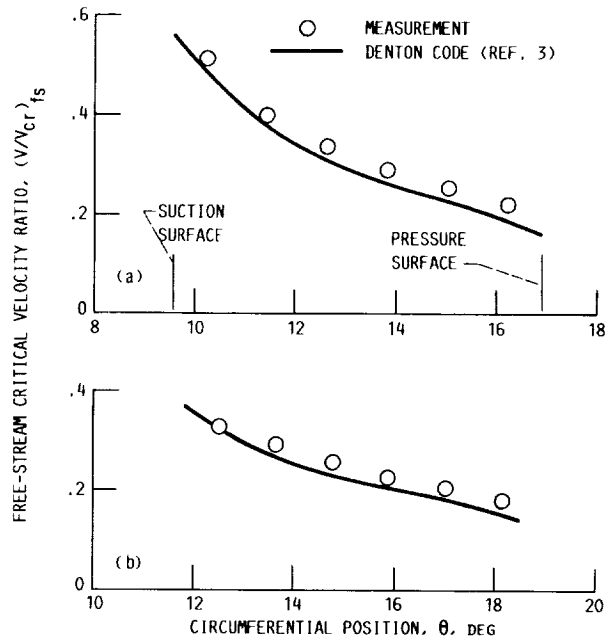

(a) Tip end wall.
(b) Hub end wall.

Figure 18.—Distribution of free-stream critical velocity ratio on end walls at an axial position of 20-percent axial chord and a pressure ratio, $p_{h,M}/P_0$, of 0.724. (Velocities calculated from surface static pressure measurements.)

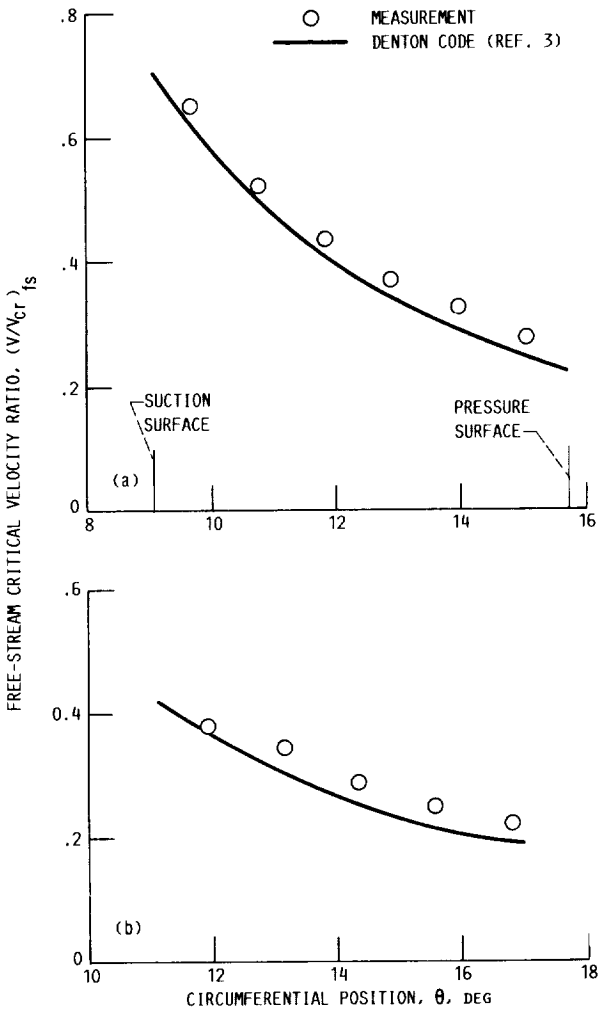

(a) Tip end wall.
(b) Hub end wall.

Figure 19.—Distribution of free-stream critical velocity ratio on end walls at an axial position of 40-percent axial chord and a pressure ratio, $p_{h,M}/P_0$, of 0.724. (Velocities calculated from surface static pressure measurements.)

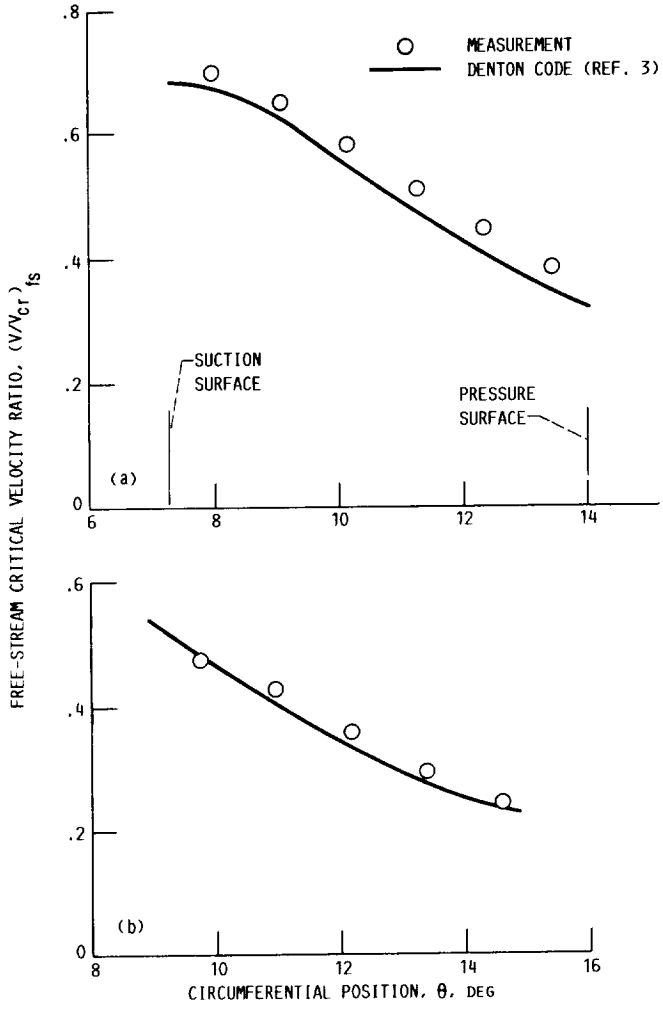

(a) Tip end wall.
(b) Hub end wall.

Figure 20.—Distribution of free-stream critical velocity ratio on end walls at an axial position of 60-percent axial chord and a pressure ratio, $p_{h,M}/P_0$, of 0.724. (Velocities calculated from surface static pressure measurements.)

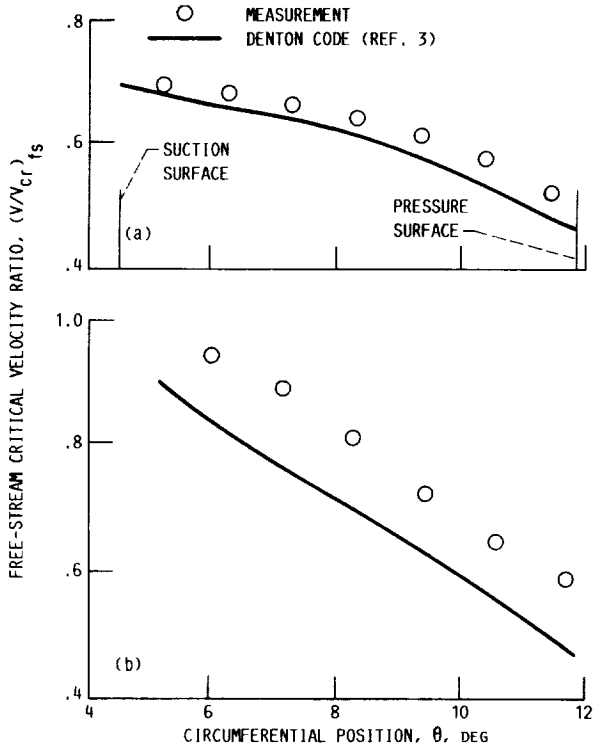

(a) Tip end wall.
(b) Hub end wall.

Figure 21.—Distribution of free-stream critical velocity ratio on end walls at an axial position of 80-percent axial chord and a pressure ratio, $p_{h,M}/P_0$, of 0.724. (Velocities calculated from surface static pressure measurements.)

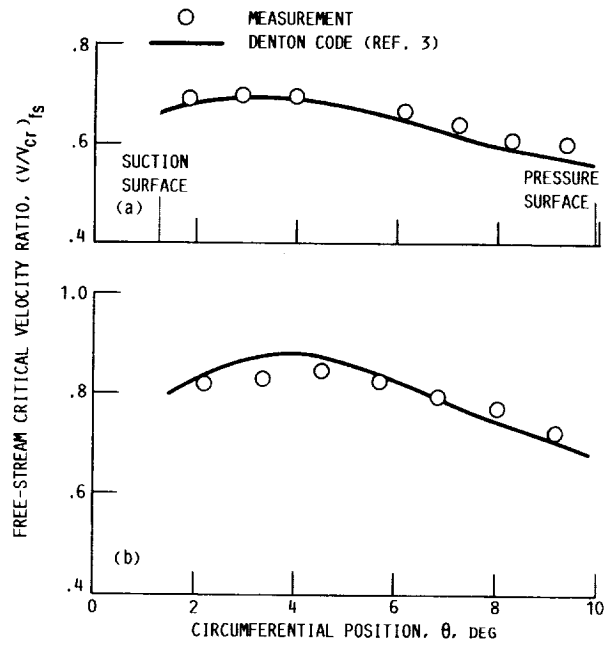

(a) Tip end wall.
(b) Hub end wall.

Figure 22.—Distribution of free-stream critical velocity ratio on end walls at an axial position of 95-percent axial chord and a pressure ratio, $p_{h,M}/P_0$, of 0.724. (Velocities calculated from surface static pressure measurements.)

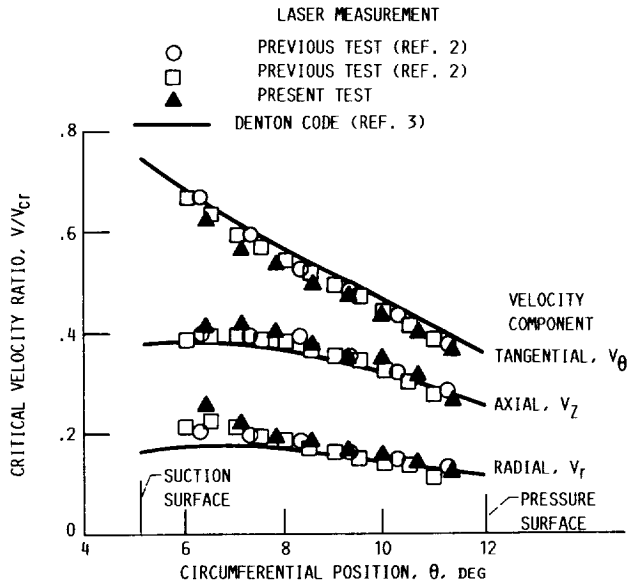

Figure 23.—Comparison of laser measurements with previous results at 80-percent axial chord. Radial position R, 10-percent span.

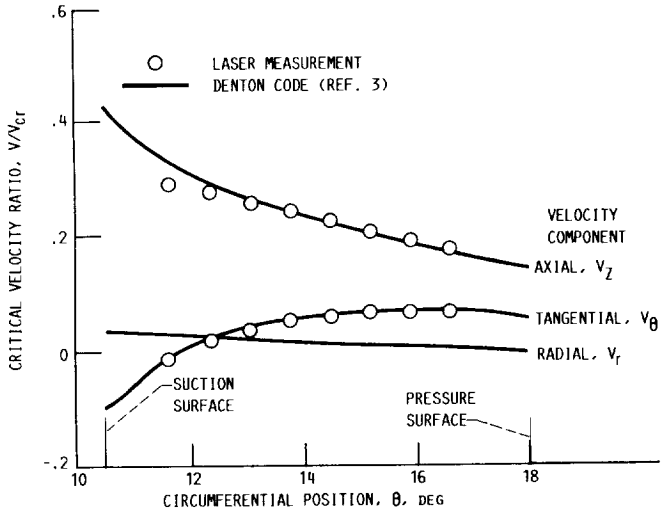

Figure 24.—Comparison of laser measurements with theory at 10-percent axial chord. Radial position R, 50-percent span.

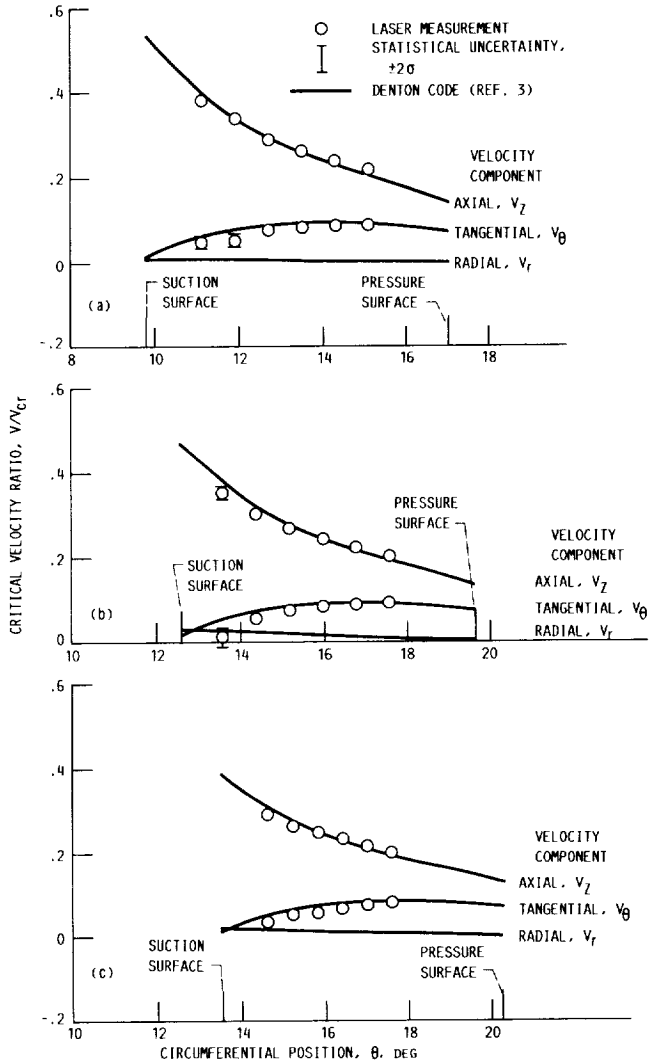

(a) Radial position R, 90-percent span.
(b) Radial position R, 50-percent span.
(c) Radial position R, 10-percent span.

Figure 25.—Comparison of laser measurements with theory at 20-percent axial chord.

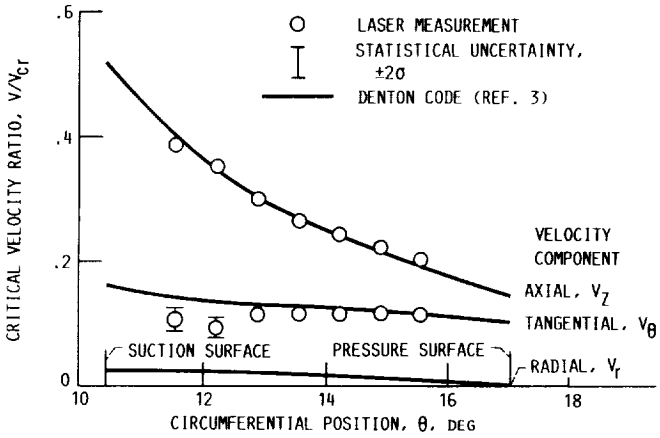

Figure 26.—Comparison of laser measurements with theory at 30-percent axial chord. Radial position R, 50-percent span.

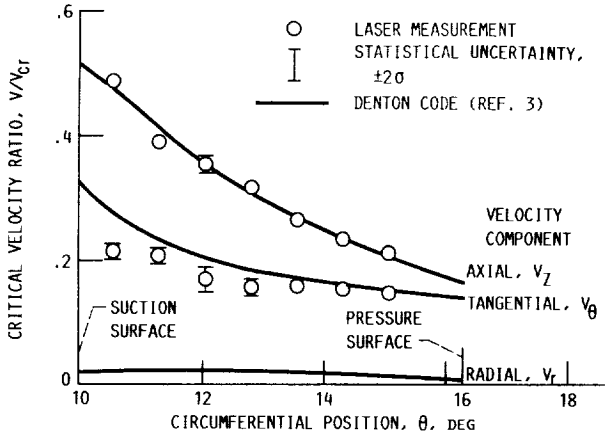

Figure 27.—Comparison of laser measurements with theory at 40-percent axial chord. Radial position R, 50-percent span.

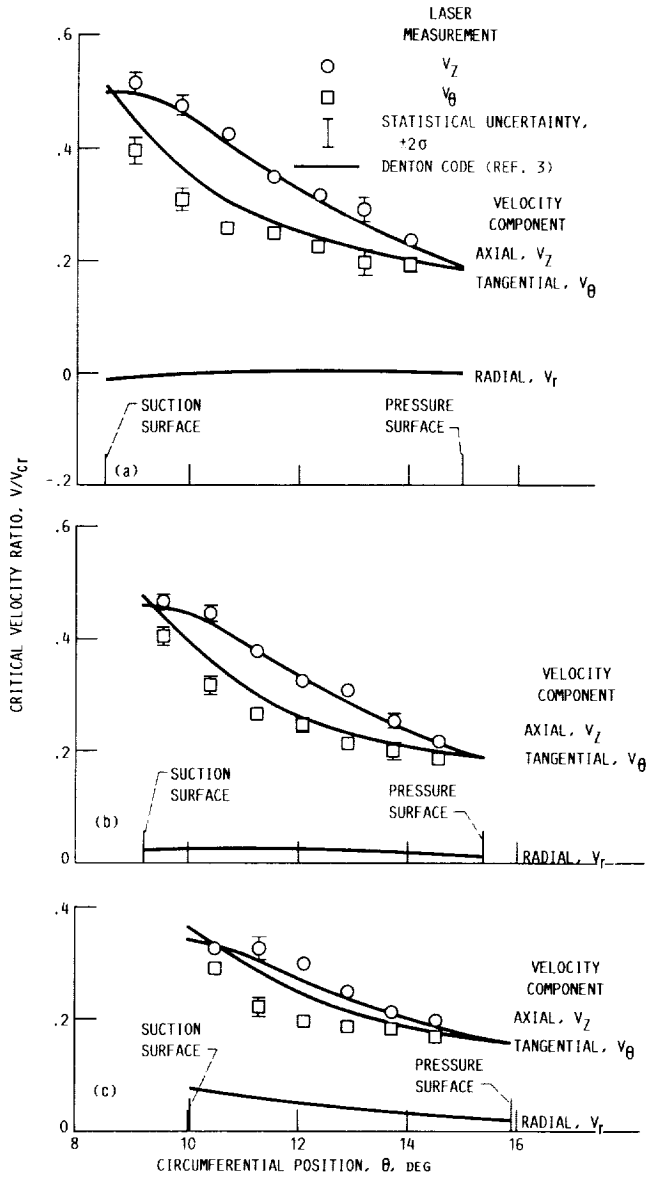

(a) Radial position R, 90-percent span.
(b) Radial position R, 50-percent span.
(c) Radial position R, 10-percent span.

Figure 28.—Comparison of laser measurements with theory at 50-percent axial chord.

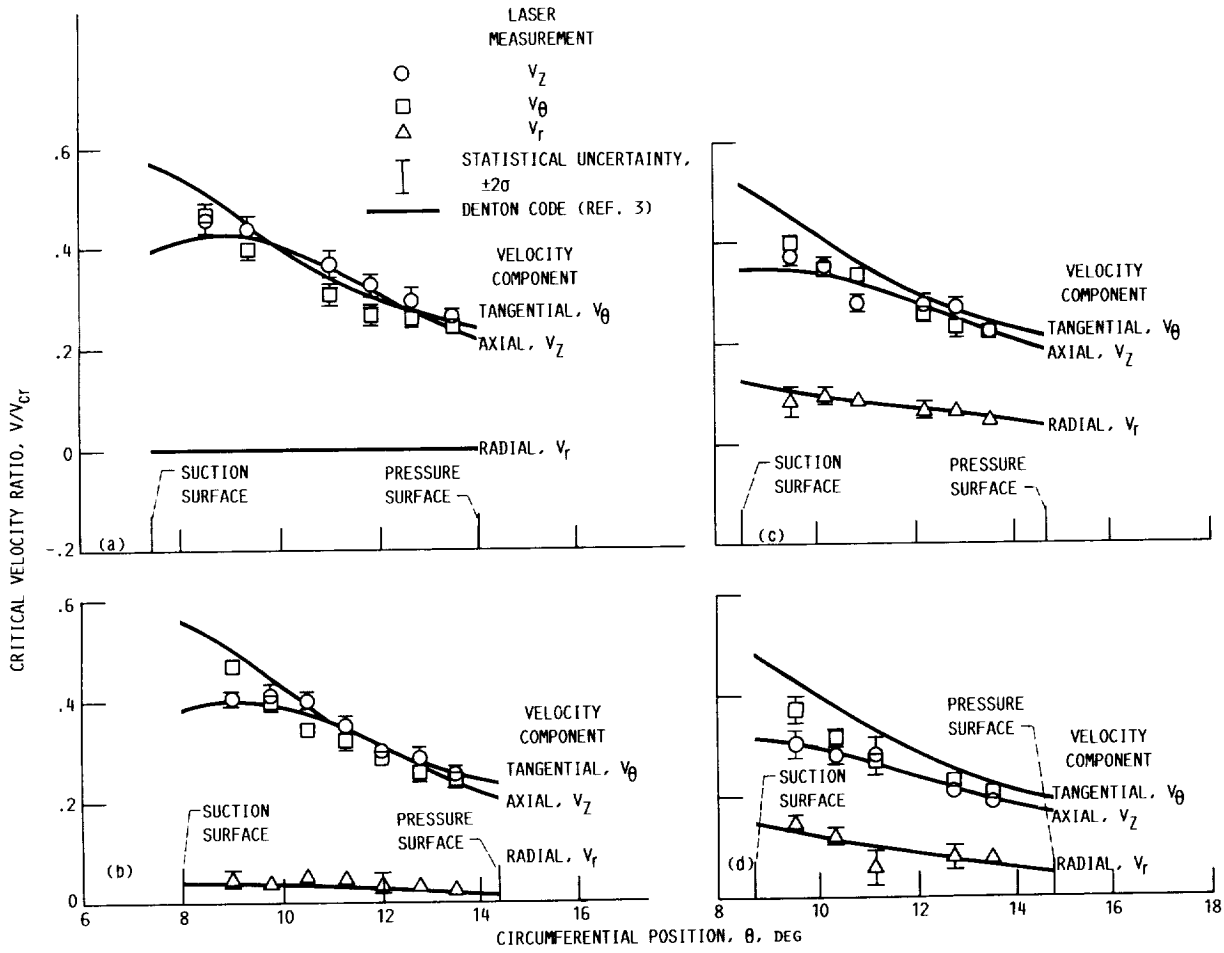

(a) Radial position R, 90-percent span.
(b) Radial position R, 50-percent span.
(c) Radial position R, 20-percent span.
(d) Radial position R, 10-percent span.

Figure 29.—Comparison of laser measurements with theory at 60-percent axial chord.

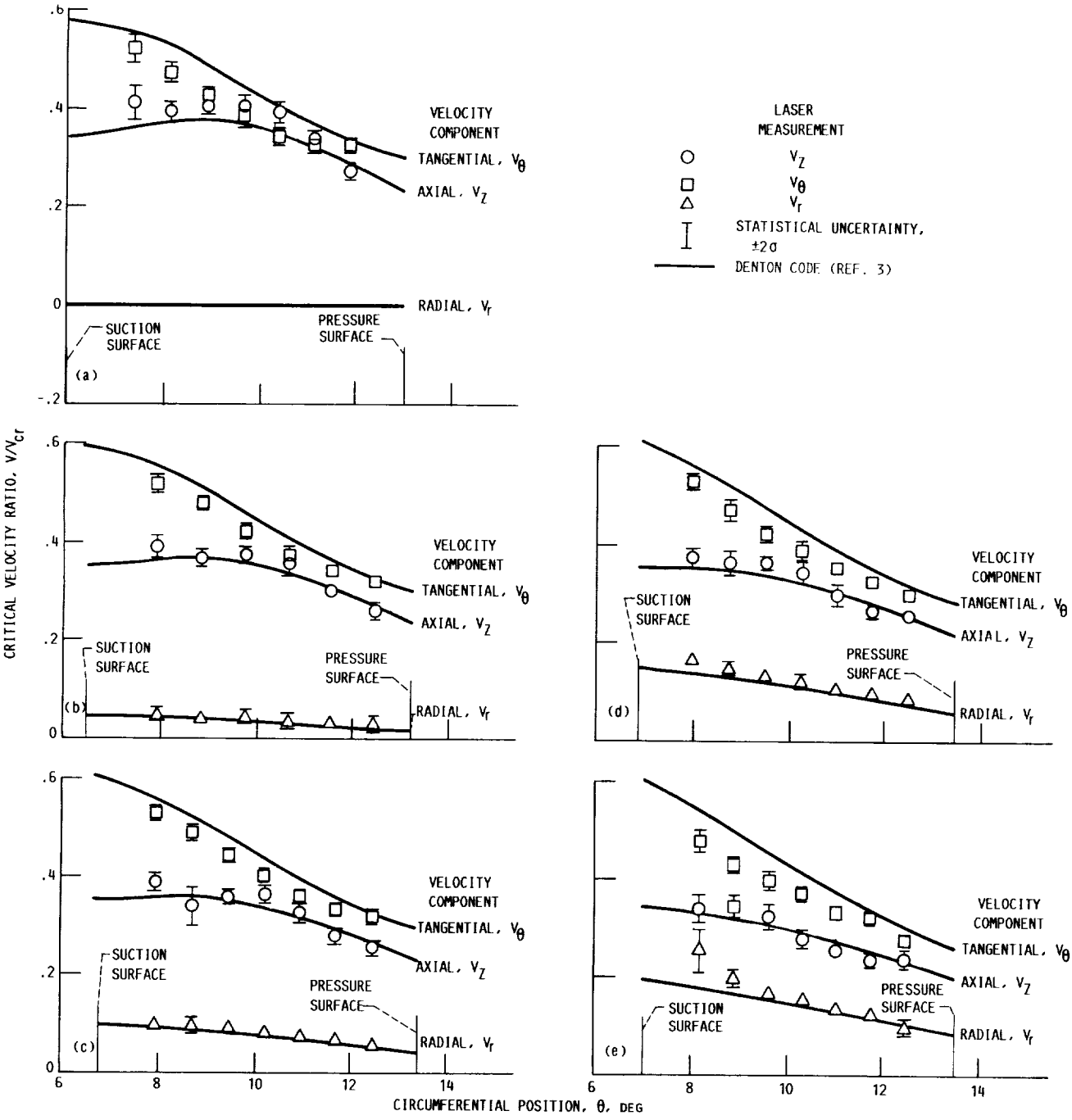

(a) Radial position R, 90-percent span.
(b) Radial position R, 50-percent span.
(c) Radial position R, 30-percent span.
(d) Radial position R, 20-percent span.
(e) Radial position R, 10-percent span.

Figure 30.—Comparison of laser measurements with theory at 70-percent axial chord.

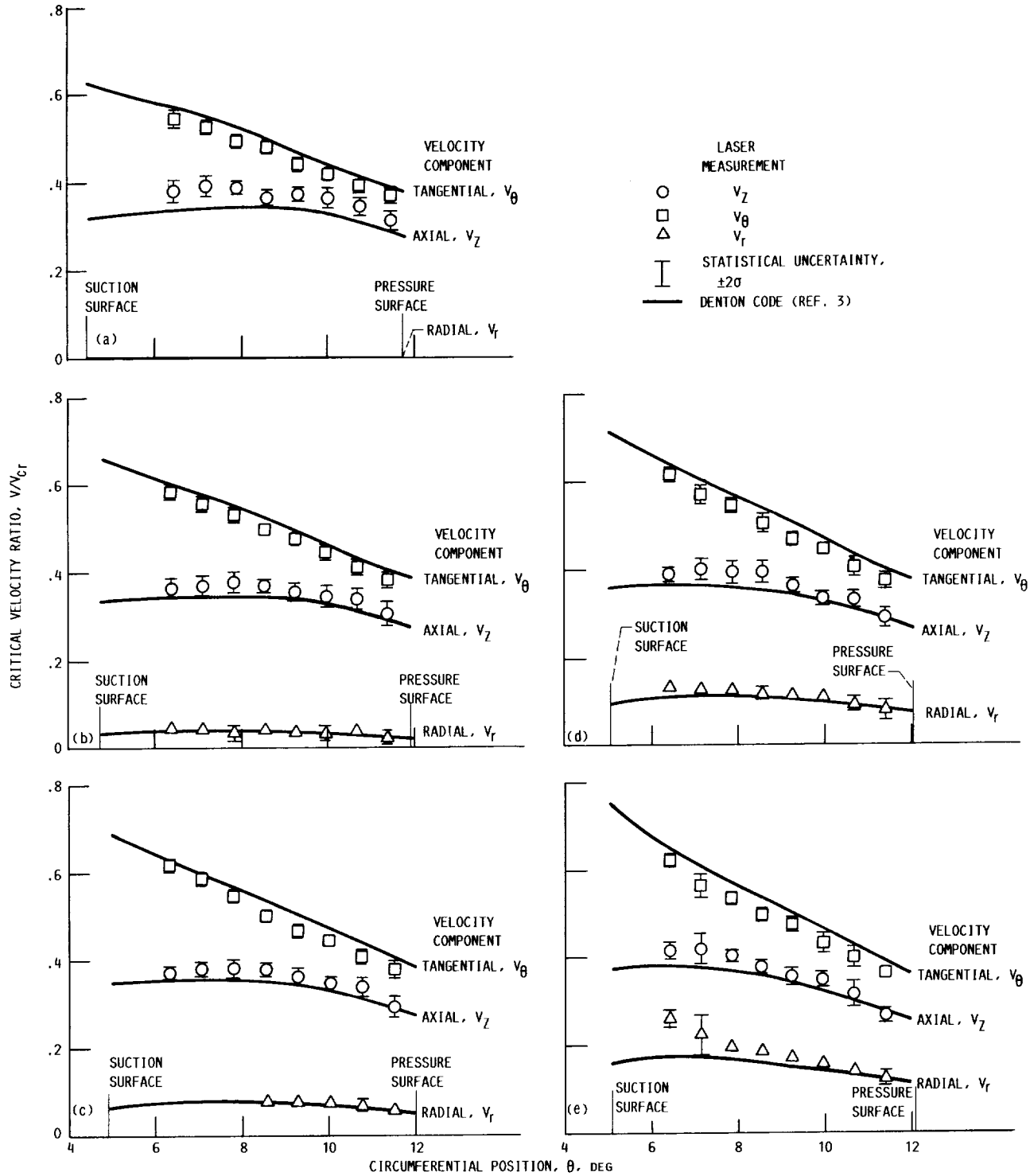

(a) Radial position R, 90-percent span.
(b) Radial position R, 50-percent span.
(c) Radial position R, 30-percent span.
(d) Radial position R, 20-percent span.
(e) Radial position R, 10-percent span.

Figure 31.—Comparison of laser measurements with theory at 80-percent axial chord.

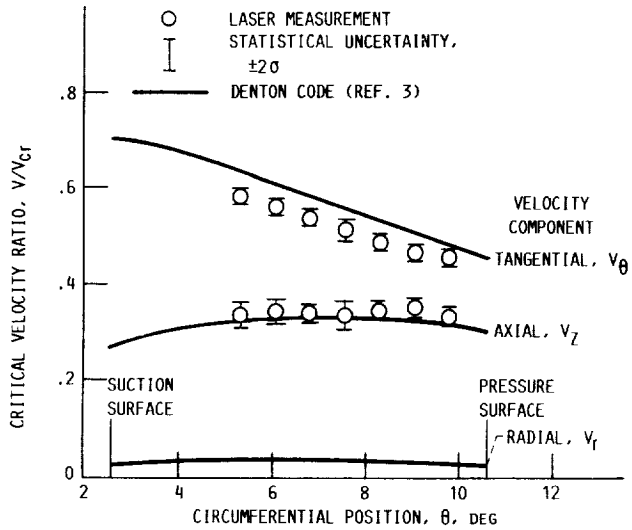

Figure 32.—Comparison of laser measurements with theory at 90-percent axial chord. Radial position *R*, 50-percent span.

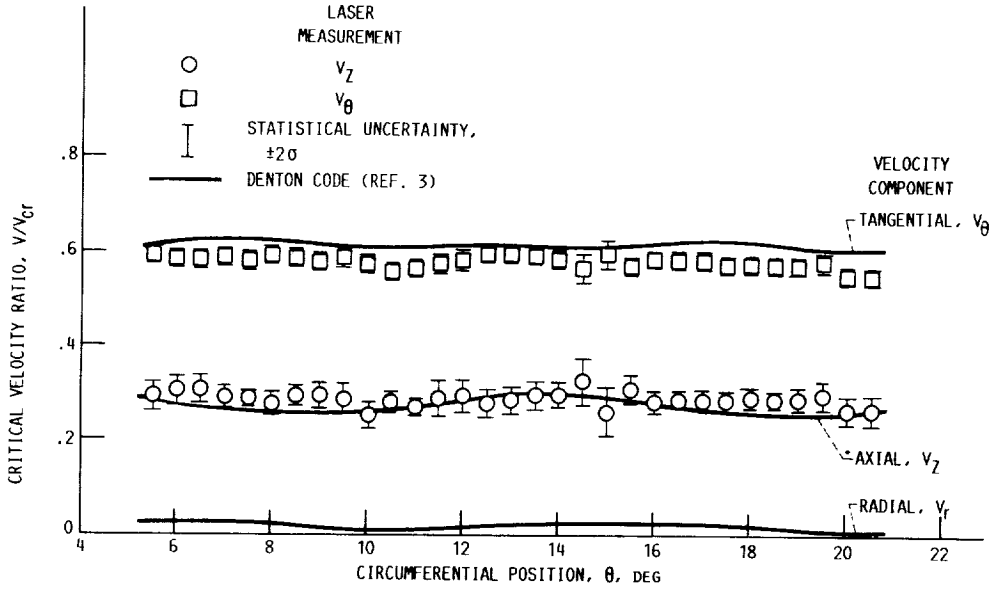

Figure 33.—Comparison of laser measurements with theory at 150-percent axial chord. Radial position *R*, 50-percent span.

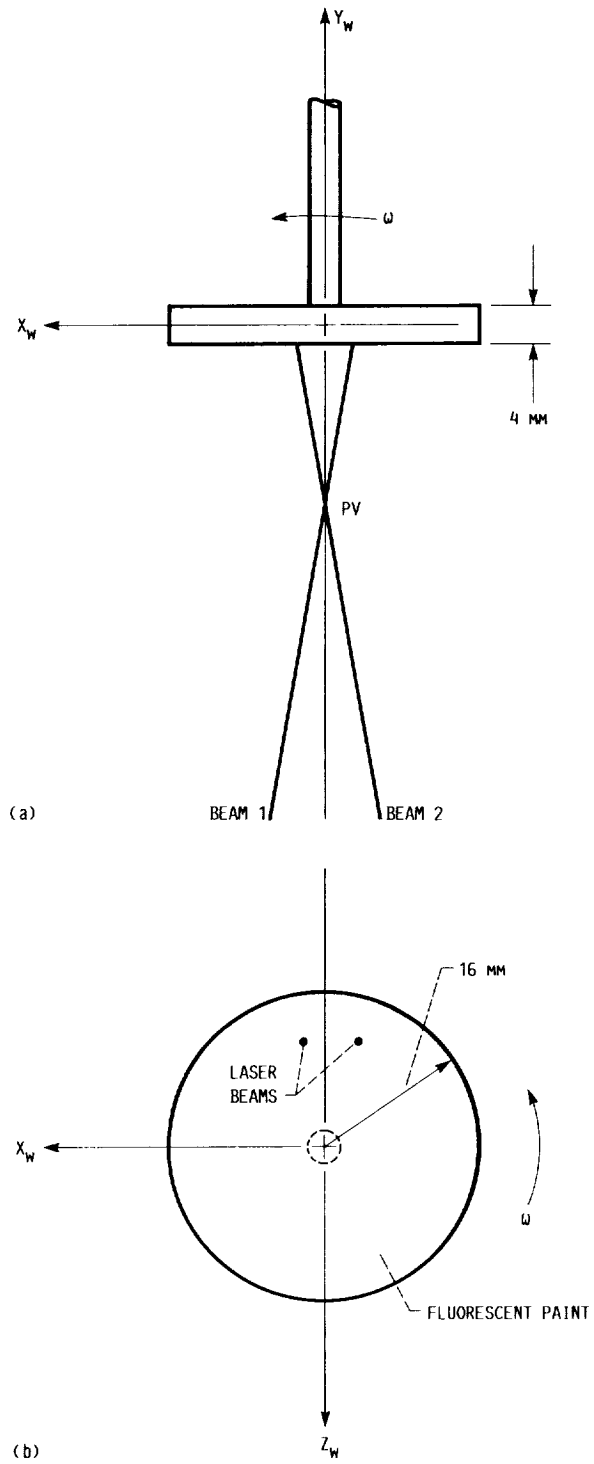

(a) Top view.
(b) Front view.

Figure 34.—Rotating wheel geometry for adjusting pinholes in optical configuration.

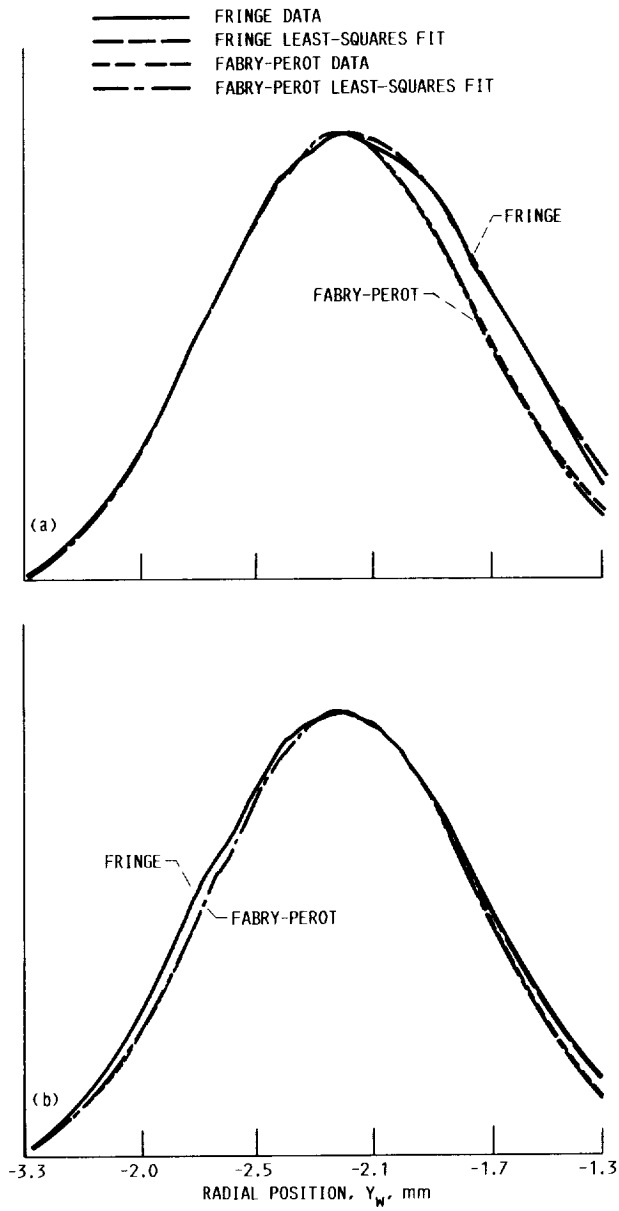

(a) Before adjustment of fringe system pinhole. (Probe volume offset 47 μm.)
(b) After adjustment of fringe system pinhole. (Probe volume offset 2 μm.)

Figure 35.—Determination of effective probe volume locations of fringe and Fabry-Perot receiving optics with rotating target.

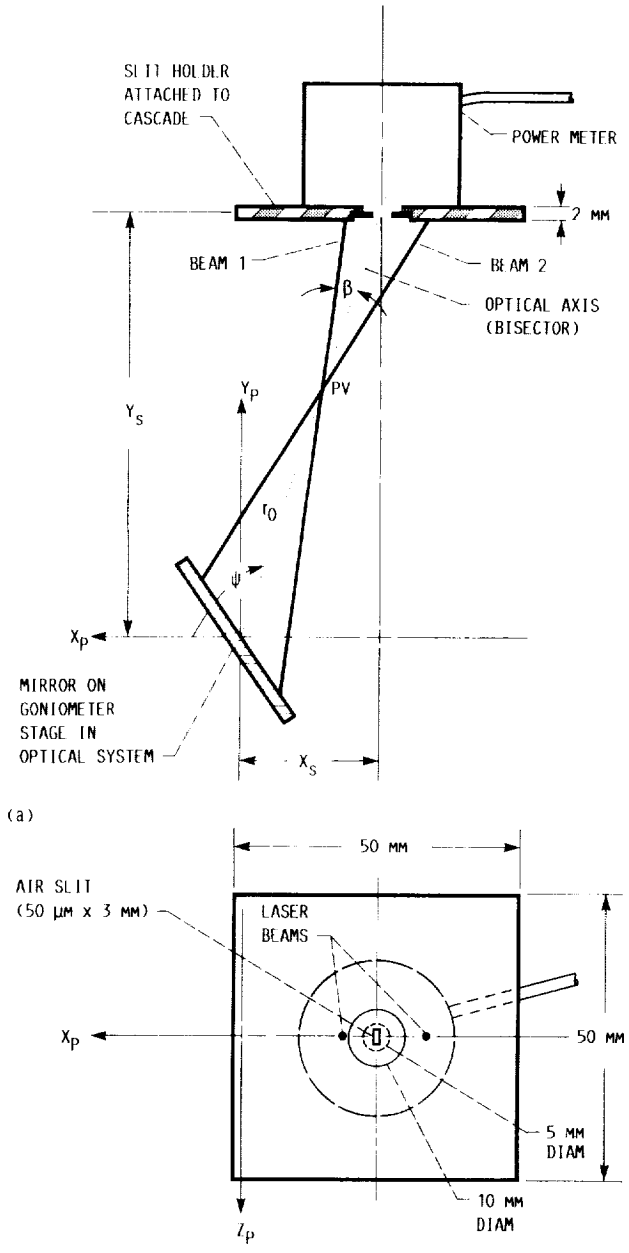

(a) Top view.
(b) Front view.

Figure 36.—Air slit geometry used for calibration of goniometric stage. (Beams in horizontal plane.)

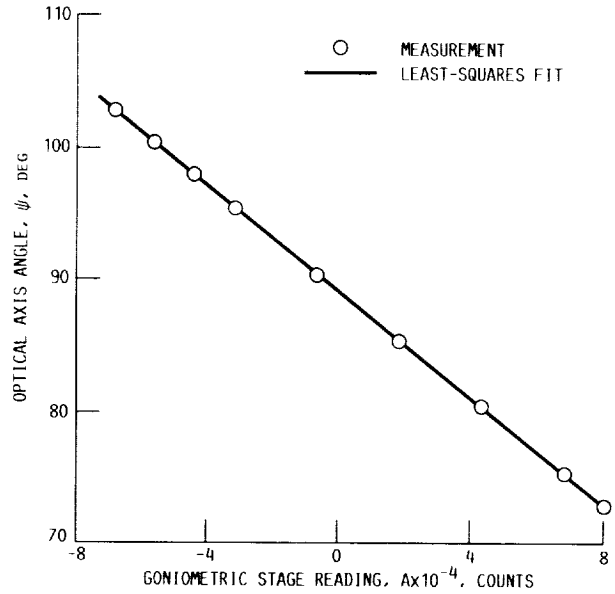

Figure 37.—Goniometric stage calibration.

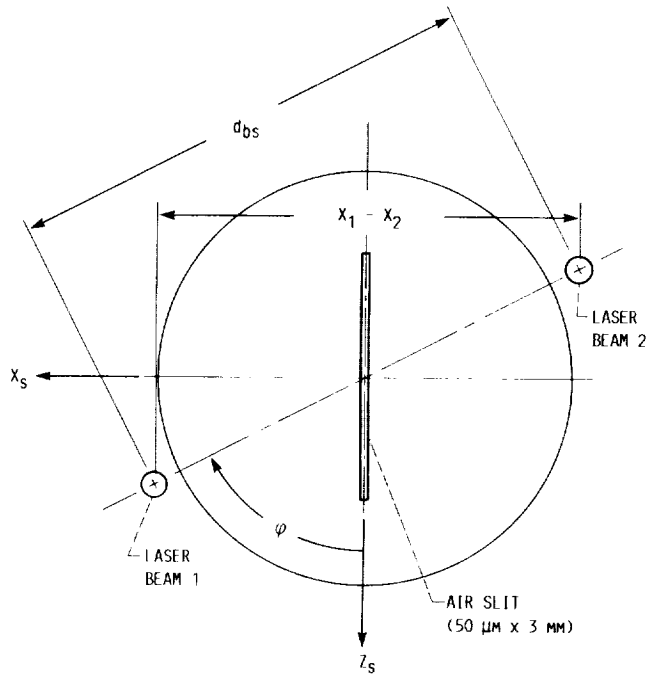

Figure 38.—Air slit geometry used for calibration of beam divider stage. (Optical axis perpendicular to slit, $\psi = 90°$.)

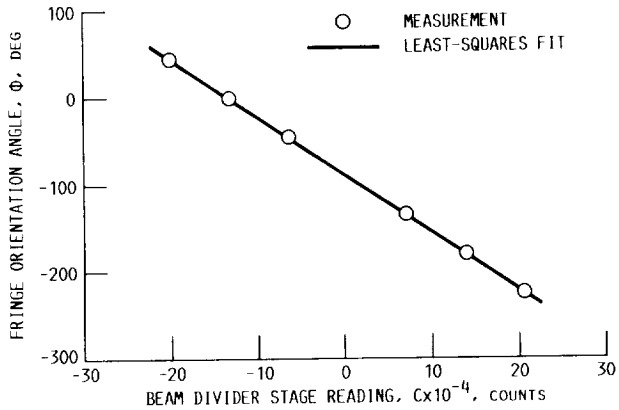

Figure 39.—Beam divider stage calibration.

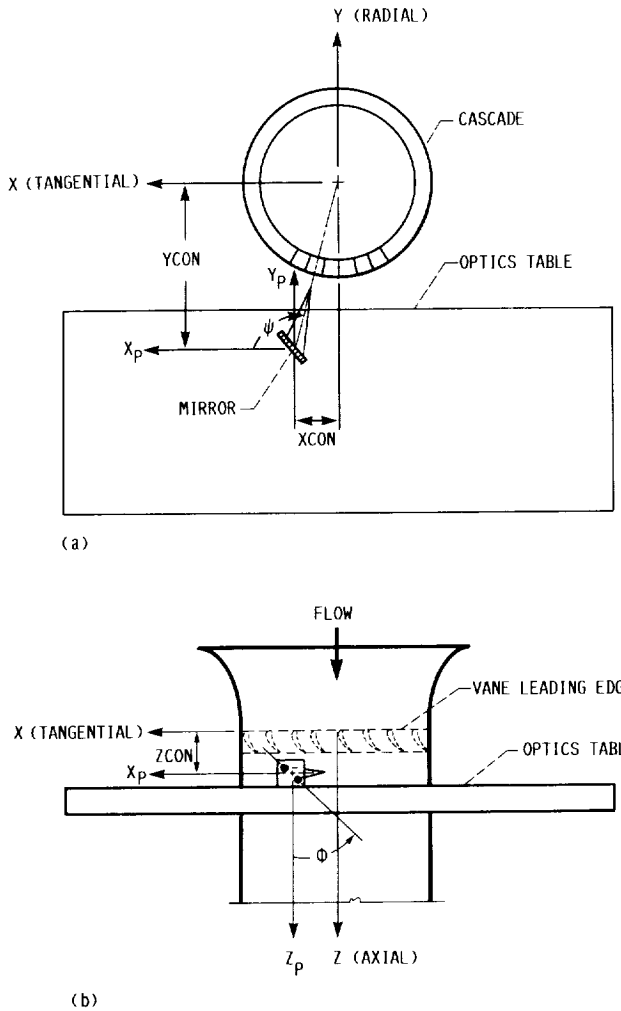

(a) Top view.
(b) Front view.

Figure 40.—Cascade and optics positioner coordinate system.

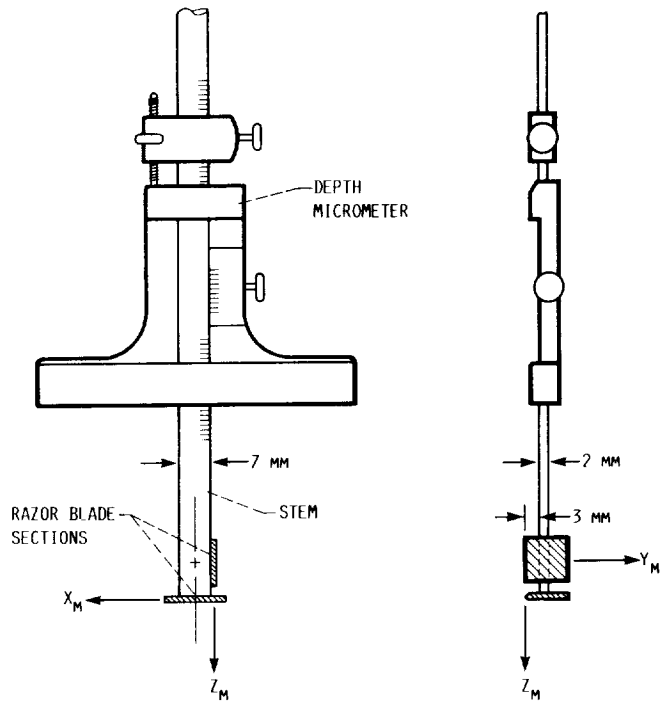

(a) Front view.
(b) Side view.

Figure 41.—Depth micrometer and razor blade sections used to determine the relationship between the cascade and optics positioning system axes.

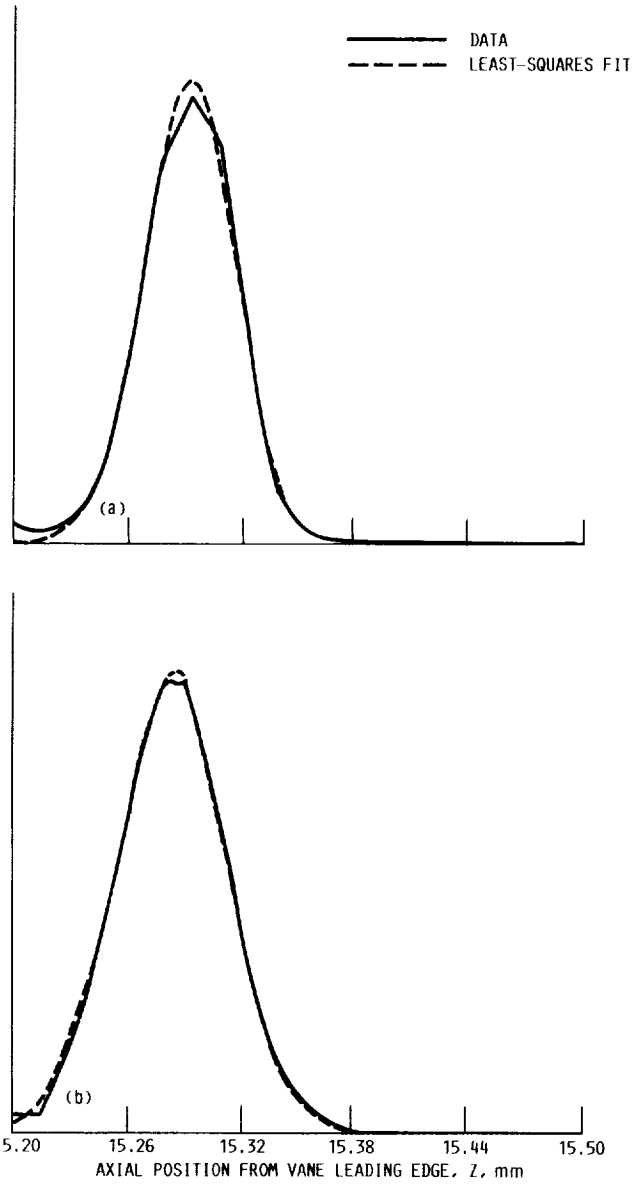

(a) Scan at $\theta = 267.5°$; peak location, 15.291 mm.
(b) Scan at $\theta = 268.9°$; peak location, 15.283 mm.

Figure 42.—Determination of relative position of cascade and optics positioning system axes using razor blade scans.

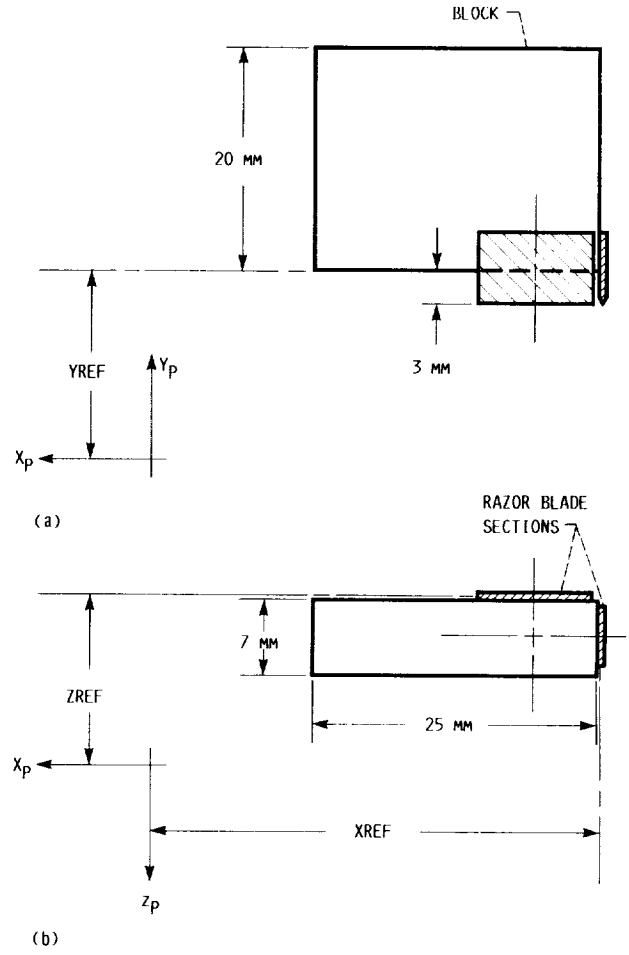

(a) Top view.
(b) Front view.

Figure 43.—Block and razor blade sections used to determine the relative position of the cascade and optics positioning systems during cascade operation.

NASA
National Aeronautics and Space Administration

Report Documentation Page

1. Report No.	2. Government Accession No.	3. Recipient's Catalog No.
NASA TP-2846		

4. Title and Subtitle	5. Report Date
Three Component Laser Anemometer Measurements in an Annular Cascade of Core Turbine Vanes With Contoured End Wall	November 1988
	6. Performing Organization Code

7. Author(s)	8. Performing Organization Report No.
Louis J. Goldman and Richard G. Seasholtz	E-4183
	10. Work Unit No. 505-62-21

9. Performing Organization Name and Address	11. Contract or Grant No.
National Aeronautics and Space Administration Lewis Research Center Cleveland, Ohio 44135-3191	
	13. Type of Report and Period Covered: Technical Paper

12. Sponsoring Agency Name and Address	14. Sponsoring Agency Code
National Aeronautics and Space Administration Washington, D.C. 20546-0001	

15. Supplementary Notes

16. Abstract

The three mean velocity components have been measured in a full-scale annular turbine stator cascade with contoured hub end wall using a newly developed laser anemometer system. The anemometer consists of a standard fringe configuration using fluorescent seed particles to measure the axial and tangential components. The radial component is measured with a scanning confocal Fabry-Perot interferometer. These two configurations are combined in a single optical system that can operate simultaneously in a backscatter mode through a single optical access port. Experimental measurements were obtained both within and downstream of the stator vane row and compared with calculations from a three-dimensional inviscid computer program. In addition, detailed calibration procedures are described that were used, prior to the experiment, to accurately determine the laser beam probe volume location relative to the cascade hardware.

17. Key Words (Suggested by Author(s))	18. Distribution Statement
Laser fringe anemometer; Fabry-Perot interferometer; Annular turbine stator cascade; Three-dimensional velocity measurements; Experimental and analytical comparisons; Calibration techniques	Unclassified – Unlimited Subject Category 02

19. Security Classif. (of this report)	20. Security Classif. (of this page)	21. No of pages	22. Price*
Unclassified	Unclassified	44	A03

NASA FORM 1626 OCT 86

*For sale by the National Technical Information Service, Springfield, Virginia 22161

NASA-Langley, 1988

National Aeronautics and
Space Administration
Code NTT-4

Washington, D.C.
20546-0001

NASA